

Noise-Resilient Quantum Evolution in Open Systems through Error-Correcting Frameworks

Nirupam Basak,^{1,*} Goutam Paul,^{1,†} and Pritam Chattopadhyay^{2,‡}

¹Indian Statistical Institute, Kolkata 700108, India

²Weizmann Institute of Science, Rehovot 7610001, Israel

(Dated: January 16, 2026)

We analyze quantum state preservation in open quantum systems using quantum error-correcting (QEC) codes that are explicitly embedded into microscopic systembath models. Instead of abstract quantum channels, we consider multi-qubit registers coupled to bosonic thermal environments, derive a second-order master equation for the reduced dynamics, and use it to benchmark the five-qubit, Steane, and toric codes under local and collective noise. We compute state fidelities for logical qubits as functions of coupling strength, bath temperature, and the number of correction cycles. In the low-temperature regime, we find that repeated error-correction with the five-qubit code strongly suppresses decoherence and relaxation, while in the high-temperature regime, thermal excitations dominate the dynamics and reduce the benefit of all codes, though the five-qubit code still outperforms the Steane and toric codes. For two-qubit Werner states, we identify a critical evolution time before which QEC does not improve fidelity, and this time increases as entanglement grows. After this critical time, QEC does improve fidelity. Comparative analysis further reveals that the five-qubit code (the smallest perfect code) offers consistently higher fidelities than topological and concatenated architectures in these open-system settings. These findings establish a quantitative framework for evaluating QEC under realistic noise environments and provide guidance for developing noise-resilient quantum architectures in near-term quantum technologies.

I. INTRODUCTION

Quantum computing (QC) technologies have rapidly evolved, heralding transformative potential across computational and information-processing domains [1–5]. The theoretical promise of quantum speedup is now being substantiated through practical demonstrations on first-generation *quantum processors* [6, 7]. However, transitioning from these early-stage *noisy intermediate-scale quantum* (NISQ) devices [8–11] to scalable, fault-tolerant quantum architectures remains an immense challenge. At the heart of this challenge lies the urgent need to mitigate the detrimental impact of environmental noise and system imperfections. Both quantum error correction (QEC) [12–61] and fault tolerance [62–73] are essential pillars for the reliable execution of quantum information processing (QIP) tasks, but they demand sophisticated theoretical frameworks and precise experimental implementation.

QEC, introduced independently by Shor [12] and Steane [13], provides a structured methodology to safeguard quantum information from *decoherence* and other forms of noise-induced degradation [12, 15, 17–20, 26, 46, 50, 74–76]. Despite formidable experimental hurdles, several successful realizations of QEC codes have been demonstrated using current quantum technologies [27, 31, 37, 41, 42, 77–79].

Traditionally, QEC strategies [12–15, 17–20, 26, 40, 46, 50, 74, 75] are analyzed using abstract quantum channel models, which encapsulate noise effects without explicitly modeling the underlying physical interactions. However, these channels often emerge as approximations to more fundamental Hamiltonian noise models, where the quantum system is coupled to an inaccessible bath, and the dynamics are governed by

system-bath interactions [80]. While quantum circuits dominated by Markovian noise exhibit higher error thresholds and tractable correction strategies, more general, non-Markovian noise scenarios remain challenging. This raises a crucial question: *Are the simplified noise models typically used in QEC studies adequate for describing realistic, physically grounded quantum noise?*

In the broader context of quantum theory, virtually every quantum system is intrinsically susceptible to the influence of its surrounding environment, commonly referred to as the bath [80]. The ensuing interaction results in the inevitable and irreversible degradation of quantum coherence due to decoherence. Far from being a mere technical nuisance, decoherence plays a foundational role in shaping the thermodynamic behavior of open quantum systems (OQSs). It is regarded as the physical mechanism that underlies the emergence of the *time arrow*, manifesting through an increase in entropy and the suppression of coherent dynamics [81–87].

This irreversible loss of coherence stands as a principal barrier to the advancement of quantum technologies. It undermines the delicate quantum superpositions required for the reliable operation in quantum computing processes [4, 88], reduces the fidelity of quantum communication protocols [4, 89], and severely limits the efficacy of quantum memories and sensing [90–95]. As such, mitigating decoherence remains a central challenge for the successful realization of robust and scalable quantum information systems.

This work analyzes quantum state preservation in open quantum systems (OQSs) using realistic, physically motivated systembath models, going beyond idealized quantum-channel descriptions. We explicitly incorporate microscopic system-environment interactions and systematically benchmark the performance of quantum error-correcting (QEC) codes, namely, the five-qubit, Steane, and Toric codes, across a range of systembath coupling strengths and bath temperatures. In the low-temperature regime, we find the following.

(i) The five-qubit code provides a pronounced advantage

* nirupambasak2020@iitk.alumni.org

† goutam.paul@isical.ac.in

‡ pritam.chattopadhyay@weizmann.ac.il

over others in preserving state fidelity.

(ii) Repeated error-correction cycles efficiently suppress both decoherence and energy relaxation for weak and moderately strong couplings.

(iii) In the high-temperature regime, we observe that thermal excitations dominate the dynamics and reduce the overall effectiveness of QEC codes.

(iv) In the same regime as above, the fidelity decay for larger coupling strengths remains qualitatively similar to that observed in the weak-coupling case.

(v) Despite the above degradation, the five-qubit code consistently outperforms the Steane and toric codes.

(vi) Extending the analysis to two logical qubits, specifically two-qubit Werner states, we identify a critical evolution time before which QEC fails to improve fidelity.

(vii) This critical time increases with the degree of entanglement, indicating enhanced fragility of strongly entangled states.

Collectively, these results highlight the interplay between system-bath correlations, thermal noise, and code structure, and establish a quantitative framework for benchmarking QEC performance in realistic open-system environments, providing guidance for the design of noise-resilient quantum architectures.

II. MANY-BODY SYSTEM MODEL

We consider an open quantum system comprising a two-qubit logical register and a variable number of ancilla qubits, the latter depending on the specific QEC code under investigation (e.g., five-qubit, Steane, or Toric code). The logical and ancilla qubits together form what we denote as the total system. Each qubit in this system interacts with its own independent local/collective environment (Fig. 1), modeled as a bosonic bath, thereby introducing decoherence and dissipation characteristic of OQSs.

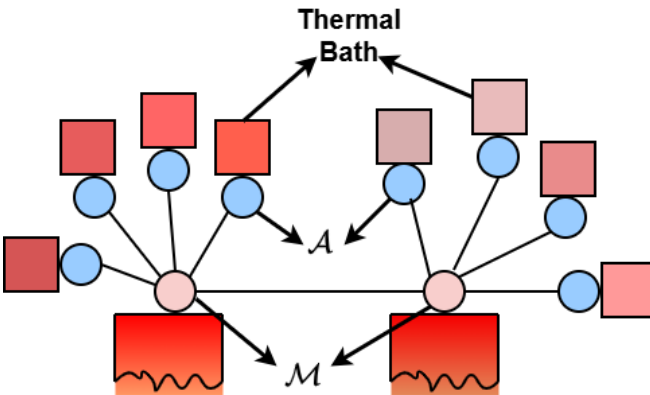


Figure 1. Schematic of the system-ancilla and its respective thermal baths. \mathcal{A} denotes the ancilla for the respective main qubit \mathcal{M} . The ancilla and the system qubit interact with local thermal baths with different temperatures. The different shades of red are used to designate the different temperatures of the thermal bath.

The complete Hamiltonian governing the *system-bath dynamics* [80, 96] is expressed as a sum over local contributions from each qubit:

$$H = \sum_j H_j^S + H_j^B + H_j^{SB}, \quad (1)$$

where the index j runs over all qubits (both logical and ancillary) in the total system. Each qubit (system-ancilla) j evolves under a local Hamiltonian H_j^S ($S = \mathcal{M}\text{-}\mathcal{A}$, \mathcal{M} and \mathcal{A} denotes the main system and ancilla qubits, respectively.):

$$H_j^S = \frac{\omega_j}{2} \hat{\sigma}_{zz}, \quad (2)$$

where ω_j is the frequency of the qubit j , $\hat{\sigma}_{\gamma j}$ ($\gamma = x, y, z$) are the Pauli operators. This term encapsulates the free evolution of individual qubits under their respective quantization axes and sets the energy scale for their dynamics in the absence of interactions.

The bath Hamiltonian H_j^B reads as

$$H^B = \sum_j \hat{H}_j^B = \sum_j \sum_k \Omega_{k,j} b_{k,j}^\dagger b_{k,j}, \quad (3)$$

where $\Omega_{k,j}$ denotes the frequency of the k th mode of the j th bath, $b_{k,j}^\dagger$ and $b_{k,j}$ represents the creation and the annihilation operators respectively. The bath is initially in a thermal equilibrium state: $\rho_B = e^{-\beta H^B} / Z$, where β and Z characterize the inverse temperature and partition function of the bath.

The bosonic bath weakly interacts with system-ancilla spins. The coupling Hamiltonian yields as

$$H_j^{SB} = \sum_k g_{k,j} \left(\sigma_j^+ b_{k,j} + \sigma_j^- b_{k,j}^\dagger \right), \quad (4)$$

where $g_{k,j}$ denotes the coupling strength of the j th qubit to the bosonic bath modes. The spin ladder operators σ_j^\pm correspond to the qubit raising and lowering operators, facilitating energy exchange between the system and the reservoir.

Here, we assume that the system qubits and the ancilla are coupled during the time evolution. Therefore, the dynamics of the system-ancilla are described using the master equation method.

Bath-driven evolution of the system-ancilla

To describe the dynamics of an OQS under weak coupling to its environment, we employ a time-nonlocal master equation for the reduced density matrix $\rho_S(t)$ of the system. The full system-bath interaction is treated perturbatively up to second order in the interaction Hamiltonian H_{SB} , which is valid in the Born approximation. Throughout the analysis we will restrict ourselves to *weak to moderate coupling*, with $\kappa/\omega \leq 0.1$, so that the second-order Born approximation remains qualitatively valid; $\kappa = 0.01\omega$ and $\kappa = 0.1\omega$ are used to represent relatively weaker and stronger couplings within this regime. The resulting integro-differential master equation

reads:

$$\begin{aligned}\dot{\rho}_S(t) &= -i[H_S(t), \rho_S(t)] \\ &+ \int_{t'=0}^t dt' \Phi(t-t')[S(t)\rho_S(t), S(t')] + h.c.\end{aligned}\quad (5)$$

$\Phi(t-t')$ is the bath correlation function encapsulating the memory effects of the environment, $H_S(t)$ is the system hamiltonian and $S(t)$ denotes the system operator coupled to the bosonic bath in the interaction picture. Eq. (5) emerges from tracing out the bath degrees of freedom under the assumption that the bath remains in thermal equilibrium throughout the evolution.

In the interaction picture, one can derive the density matrix of the system, $\rho_S(t)$, under the assumption of the weak system-bath interaction, to second order in H_{SB} [80]. In the interaction picture, the coupling Hamiltonian becomes

$$H_{SB}^I(t) = \sum_{\alpha=1}^2 S_{\alpha}(t) \otimes B_{\alpha}^{\dagger}(t), \quad (6)$$

with $S_{\alpha}(t) = e^{iH_{St}} \tilde{S}_{\alpha} e^{-iH_{St}}$ (where $\tilde{S}_{1(2)} = \sum_i \sigma_i^{+(-)}$) and $B_{\alpha}(t) = e^{iH_B t} \tilde{B}_{\alpha} e^{-iH_B t}$ (where $\tilde{B}_{1(2)} = \sum_k g_k \sigma_k^{-(+)}$). The couplings considered here are $\tilde{B}_1 = \sum_k g_{kj} b_{kj}^{\dagger}$ and $\tilde{B}_2 = \tilde{B}_1^{\dagger}$. The bath response functions $\Phi_{\alpha\alpha'}(\tau) = \text{Tr}_B(B_{\alpha}(\tau)B_{\alpha'}(0)\rho_B)$ are shown to be of the following forms (see Appendix A)

$$\begin{aligned}\Phi_{11}(\tau) &= \Phi_{22}(\tau) = 0, \\ \Phi_{12}(\tau) &= \Gamma \langle e^{2i\omega\tau} (n(\omega) + 1) \rangle, \quad \Phi_{21}(\tau) = \Gamma \langle e^{-2i\omega\tau} n(\omega) \rangle,\end{aligned}\quad (7)$$

with $\Gamma = \sum_k g_{k,j}^2$, a positive prefactor that depends on the nature of the interaction between the bath and the system, and $n(\omega)$ is the mean occupation number of the bath mode at frequency ω . Eq. (7) reflects energy exchange between the system and the environment.

The time-evolved system operators appearing in the master equation are explicitly:

$$\begin{aligned}S_1(t) &= U_S^{\dagger}(t) \left(\sum_{i=1}^N \sigma_i^+ \right) U_S(t), \\ S_2(t) &= U_S^{\dagger}(t) \left(\sum_{i=1}^N \sigma_i^- \right) U_S(t),\end{aligned}\quad (8)$$

where N is the number of main qubits and $U_S(t) = e^{-iH_{St}}$ is the unitary time evolution operator generated by the system Hamiltonian. The operators $S_{\alpha}(t)$ capture the collective raising and lowering transitions of the system qubits under time evolution, and their interactions with the bath are responsible for decoherence and population dynamics within the system

(Appendix B).

III. QUANTUM ERROR CORRECTING CODES

To mitigate the errors caused by the baths, we employ different QEC codes to estimate the success rate of the state restoration to its initial form. A generic representation of the QEC code is shown in Fig. 2. The details of the codes are described in this section.

A. Five-qubit code

To mitigate the effects of environmental decoherence, we employ the five-qubit QEC code [15], which is the smallest perfect code capable of correcting arbitrary single-qubit errors. This code requires only five physical qubits to protect one *logical qubit* from the influence of local quantum noise. Specifically, for each system qubit, four ancillary qubits are introduced to detect and correct any single-qubit error that may occur during the systems evolution.

A complete error correction cycle in this code consists of three main stages:

Encoding (\mathcal{E}): At the beginning of the qubit's time evolution, the main system qubit is coupled with the four ancillary qubits via a unitary encoding operator U . This transforms the single-qubit logical state into a five-qubit coupled codeword within the protected code space.

Error Evolution (\mathcal{E}): The five-qubit system is then exposed to environmental interactions governed by the error channel E , which simulates decoherence or noise processes due to coupling with local reservoirs. The code allows for arbitrary single-qubit errors on any of the five qubits.

Syndrome Extraction and Recovery (\mathcal{R}): Finally, the recovery operation \mathcal{R} is applied to restore the original logical state based on the extracted error syndrome. This process is implemented through the inverse of the encoding operation, U^{\dagger} , followed by local measurements on the ancillary qubits. Notably, this phase of the code does not require any additional ancillae beyond the original five qubits. The corrective action is performed on the main qubits to reverse any error that may have affected the logical qubit.

Additional procedural and technical specifics regarding the implementation of the code are provided in Appendix C.

The primary goal of this study is to assess how the five-qubit QEC code performs under realistic error conditions, specifically, when the open-system error dynamics E accurately reflect non-Markovian and multi-channel decoherence mechanisms. This represents a significant deviation from idealized or simplistic error models, which typically assume memoryless noise and overlook complex interactions with the environment.

To isolate the role of other errors, we assume ideal (perfect) encoding \mathcal{E} and recovery \mathcal{R} operations. That is, contributions from other operational error sources, such as imperfect gate applications, state preparation, or measurement

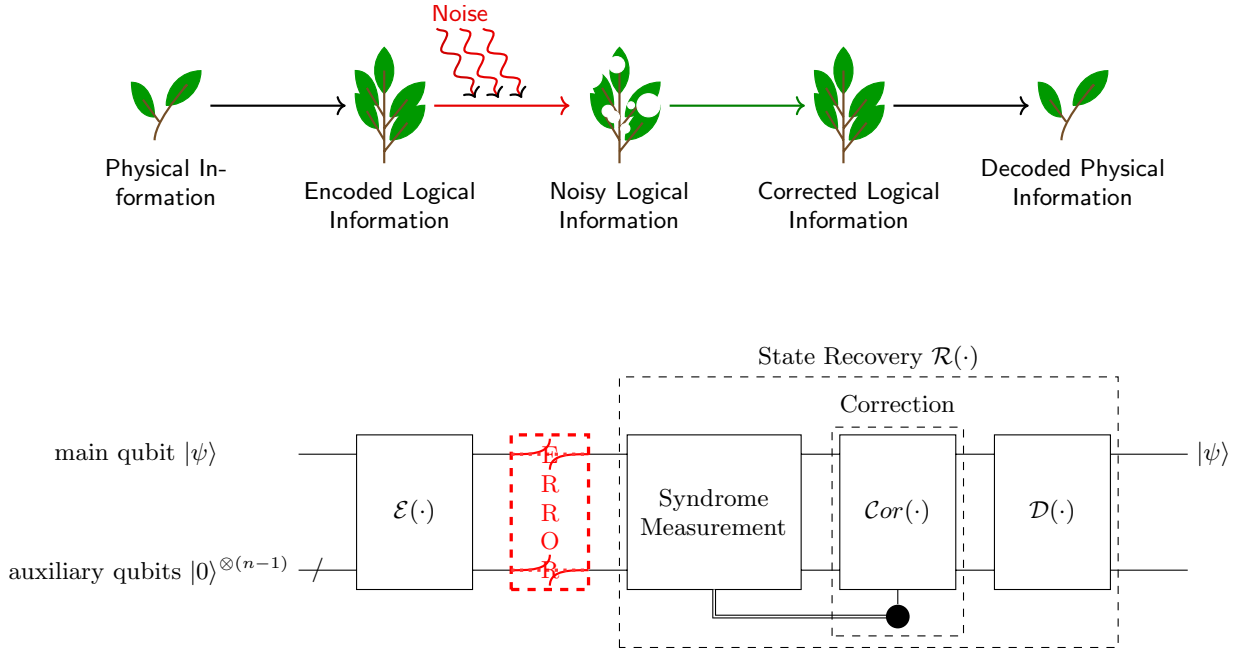


Figure 2. **(Top)** Conceptual overview of the QEC process. Physical information is encoded into logical states before the noise acts and distorts them. After passing through a correction stage, the recovered logical information is finally decoded to reproduce the original physical information. **(Bottom)** A generic block diagram for n -qubit quantum error correcting code. A physical qubit with state $|\psi\rangle$ is encoded via $\mathcal{E}(\cdot)$ with $n - 1$ auxiliary qubits initialized at state $|0\rangle$ to build one logical qubit, which undergoes some error channel, denoted in red. Then the original state is recovered via some recovery operation $\mathcal{R}(\cdot)$, which consists of syndrome measurement, i.e., correction operation $\mathcal{Cor}(\cdot)$ and decoder $\mathcal{D}(\cdot)$. By discarding the auxiliary qubits, one can get back the original state $|\psi\rangle$.

errors, are considered negligible in our modeling, consistent with assumptions in Ref. [10].

B. Steane code

To robustly counteract the effects of quantum decoherence, we implement the Calderbank-Shor-Steane (CSS) code [13, 17]: a paradigmatic class of stabilizer codes that exploits the structural richness of classical linear error-correcting codes to address quantum noise in a highly structured and modular fashion. This code enables the independent identification and correction of bit-flip (X) and phase-flip (Z) errors, thereby simplifying both analysis and practical implementation.

The CSS code encodes quantum information into a highly entangled subspace of n physical qubits, effectively distributing the logical information nonlocally and rendering it resilient against localized perturbations. This is achieved through two classical linear codes, C_1 and C_2 , satisfying the inclusion $C_2 \subset C_1$, and C_1 and C_2^\perp have minimum distance d , where C_2^\perp is the dual of C_2 . The quantum code inherits its structural and error-correcting properties from these constituent classical codes. A full CSS error correction cycle comprises the following stages:

Encoding: The logical qubit is coherently mapped onto a quantum superposition of codewords, specifically across cosets of C_2 within C_1 . This entanglement-based encoding expands the logical state into a protected subspace, wherein

error syndromes can be effectively distinguished. The encoding operation is implemented using a Clifford circuit derived from the generator matrices of the classical codes, and embeds the logical qubit into an $[\![n, k, d]\!]$ quantum code space, where $k = \dim(C_1) - \dim(C_2)$.

Error Dynamics: The encoded state is subsequently subjected to open-system dynamics modeled by a general error channel E , which encapsulates the effects of system-environment interactions. Unlike idealized depolarizing channels, our model considers more nuanced decoherence phenomena, including non-Markovian noise, correlated errors, and non-Pauli dynamics, thereby offering a more faithful depiction of realistic quantum environments.

Syndrome Extraction and Recovery: Upon exposure to noise, the system undergoes a syndrome extraction process via stabilizer measurements that diagnose the error without collapsing the encoded logical state. These stabilizers are constructed from the parity matrices of C_1 (to detect X errors) and those of C_2^\perp (to detect Z errors), enabling independent and simultaneous correction of both error types. Based on the measurement outcomes, a classical decoder determines the most probable error configuration, and a corresponding Pauli correction is applied to restore the logical state. The recovery operation \mathcal{R} thus completes the error correction cycle, with no need for auxiliary ancilla qubits beyond those used in the encoding.

The CSS code is particularly amenable to fault-tolerant implementation, as its syndrome extraction circuits can be decomposed into low-depth Clifford circuits, and it exhibits fa-

vable scaling properties when integrated into larger quantum architectures (e.g., concatenated codes or topological codes like the surface code).

In this study, our objective is to rigorously evaluate the resilience and operational fidelity of the CSS code under physically realistic noise models, surpassing the simplistic assumptions of stochastic Pauli errors that dominate much of the theoretical literature. To isolate the influence of the physical noise processes, we assume ideal encoding and recovery operations. The technical specifics regarding the implementation of the code are provided in the Appendix D.

The principal metric employed to quantify the code's efficacy is the state fidelity, which directly measures the overlap between the recovered quantum state and the original logical state. This enables a precise characterization of how well the CSS code preserves quantum coherence and information integrity under the influence of realistic environmental interactions.

C. Toric code

Unlike the five-qubit code, which minimizes qubit overhead, or the CSS code, which leverages classical code theory, the toric code [63] capitalizes on the intrinsic *topological order* of a 2D qubit lattice to encode logical qubits into nonlocal, global degrees of freedom. This structural nonlocality provides natural immunity against local errors, making the toric code inherently fault-tolerant and scalable.

The toric code is defined on an $L \times L$ square lattice with periodic boundary conditions, topologically equivalent to a torus. Qubits reside on the edges, yielding a total of $n = 2L^2$ physical qubits. The stabilizer group S_g is generated by two types of local, commuting operators: a) Star operators, $A_v = \prod_i X_i$ acting on the four edges adjacent to the vertex v . b) Plaquette operators $B_p = \prod_i Z_i$ acting on the four edges surrounding plaquette p .

The code space is the simultaneous +1 eigenspace of all stabilizers and supports $k = 2$ logical qubits. Logical operators correspond to non-contractible loops of X and Z operators encircling the torus, with code distance $d = L$, directly tied to the lattice size. This distance determines the number of detectable and correctable errors.

A complete toric code error correction cycle encompasses the following:

Encoding: The logical state is coherently mapped into the code subspace through a circuit composed of Clifford gates, initializing the stabilizers and establishing the ground-state manifold of the code Hamiltonian.

Error Dynamics: The system then evolves under the influence of an open-system noise model E , which encompasses a broad spectrum of realistic decoherence processes, ranging from temporally correlated (non-Markovian) noise to spatially correlated and non-Pauli error mechanisms, thereby offering a physically faithful representation of quantum noise in NISQ-era devices.

Syndrome Extraction and Recovery: Errors are diagnosed via local stabilizer measurements, which detect syndromes as

violations of star or plaquette conditions. These syndromes manifest as point-like anyonic excitations. A classical decoding algorithm, typically based on *minimum-weight perfect matching*, is employed to infer the most probable configuration of error chains. A suitable Pauli correction is then applied to return the state to the code subspace. Logical errors only occur if the total error chain, comprising both the actual and corrective operations, forms a topologically nontrivial loop around the torus. The technical specifics regarding the implementation of the code are provided in Appendix E.

The toric code is characterized by its scalability, locality of operations, and high error threshold, making it an archetypal platform for fault-tolerant quantum computation. In our study, we assume idealized encoding and recovery operations to isolate the influence of intrinsic decoherence mechanisms. The efficacy of the toric code under such realistic conditions is quantified via the logical fidelity, defined as the overlap between the output state and the original logical input, offering a rigorous metric for coherence preservation and the integrity of quantum information under noisy evolution.

D. Fidelity

The efficacy of all the error correction codes is quantitatively assessed by evaluating the fidelity between the recovered state and the original logical state. Fidelity serves as the key figure of merit in benchmarking the code's capacity to preserve quantum information in the presence of open-system decoherence. Let us consider a quantum channel \mathcal{C} consisting of encoding $\mathcal{E}(\bullet)$, evaluation $E(\bullet)$ and recovery $\mathcal{R}(\bullet)$. Suppose ρ_0 denotes the initial quantum state prior to the evolution, and let ρ_t denote the state of the system after it has evolved for a time t . Then we have

$$\rho_t = \mathcal{C}(\rho_0) = \mathcal{R}(E(\mathcal{E}(\rho_0))). \quad (9)$$

The state fidelity [4, 97] between ρ_0 and ρ_t is defined as

$$\mathcal{F}_{state}(\rho_0, \rho_t) = \left(\text{tr} \sqrt{\sqrt{\rho_0} \rho_t \sqrt{\rho_0}} \right)^2. \quad (10)$$

IV. STATE PRESERVATION VIA QUANTUM ERROR CORRECTION

Here, we employ the QEC codes to investigate the preservation of quantum states in open-system environments. For a comprehensive assessment of their performance, we consider two representative configurations of the logical register: one with a single logical qubit ($\mathcal{M} = 1$), corresponding to the protection of an isolated quantum state, and another with two logical qubits ($\mathcal{M} = 2$), enabling the examination of entanglement preservation and correlated error dynamics. This dual-scenario analysis allows us to elucidate how different QEC codes respond to environmental noise under varying system sizes, coupling strengths, and temperature regimes, thereby offering a unified framework for evaluating the robustness of

encoded quantum information in realistic OQSs.

A. Low-temperature Limit

In the single-qubit scenario, we employ the five-qubit QEC code to protect the initial quantum state from decoherence induced by its interaction with the environment. The study explores both weak and larger systembath coupling regimes under different noise configurations.

For the collective noise case, where both the system qubit and the ancillae are coupled to a common bath, we find that in the weak coupling regime ($\kappa = 0.01\omega$), the QEC code significantly enhances the fidelity of the stored quantum state (Fig. 3(a)). Specifically, the fidelity exhibits a steady increase with the number of QEC cycles, indicating that successive rounds of error correction effectively suppress the decoherence and energy relaxation effects arising from the systembath interaction. This demonstrates the stabilizing role of QEC in mitigating noise when the systemenvironment coupling is sufficiently weak and Markovian in nature. For a larger systembath coupling ($\kappa = 0.1\omega$), the qualitative behavior of the fidelity remains very similar to the weak-coupling case (Fig. 3(b)). Multiple QEC cycles still systematically enhance the fidelity compared with the uncorrected evolution. The stronger coupling leads to a somewhat faster decay of the bare (no-QEC) state, but this effect is largely compensated by repeated error-correction cycles, so that the net QEC advantage is comparable for both coupling strengths in the low-temperature limit.

In contrast, for local noise, where the system and each ancilla qubit interact with independent baths, the five-qubit code provides no improvement compared to the uncorrected evolution, even in the weak coupling limit. The uncorrelated nature of the local environmental interactions leads to independent error channels that are not efficiently addressed by the collective structure of the five-qubit code. Consequently, the effectiveness of QEC is limited in this regime.

Extending the analysis to the two-qubit case, we consider an initial Werner state to study the relation between entanglement and QEC performance. The results reveal a trade-off between QEC advantage and the degree of inter-qubit entanglement (Fig. 4). For weakly entangled or nearly separable states, the application of QEC substantially improves the fidelity compared to the uncorrected dynamics. As the degree of entanglement increases, however, this advantage progressively decreases and creates a small-time window where the QEC codes have less fidelity in state recovery over the uncorrected evolution. A crossover point emerges, before which the fidelity of the uncorrected evolution surpasses that of the QEC-protected case. This crossover shifts with increasing entanglement, indicating that highly entangled states couple more strongly to the environment and are therefore more challenging to stabilize using standard QEC codes. These observations highlight the intricate interplay between entanglement, environmental correlations, and the practical limits of error correction in open quantum systems.

To quantify the regime in which QEC remains beneficial for entangled inputs, in Fig. 5(a), we plot the critical value

κt_c at which the fidelity with five-qubit QEC becomes equal to the uncorrected fidelity, as a function of the mixing parameter p of the initial Werner state. For both the high- and low-temperature limit and the number of QEC cycles, κt_c sets the boundary beyond which the error-corrected evolution provides a net advantage over the bare dynamics. The curves show a systematic dependence on the degree of entanglement: as p increases and the state approaches the maximally entangled Bell state, the window in κt over which QEC improves the state shrinks, indicating that highly entangled states are more fragile to the combined action of systembath coupling and thermal noise. Increasing the number of QEC cycles shifts κt_c so that the beneficial region extends over a broader range of evolution times for all p , but it does not eliminate the overall trend that strongly entangled states are harder to protect than weakly entangled or nearly separable states using traditional QEC codes. We restrict Fig. 5(a) to the weak-coupling case $\kappa = 0.01\omega$, as the larger system-bath coupling, $\kappa = 0.1\omega$, displays very similar behavior and would not change the qualitative conclusions.

B. High-temerature limit

In this regime, the performance of the QEC code deteriorates significantly due to the enhanced thermal excitations in the environment. As the bath temperature increases, the population of higher-energy bosonic modes grows, leading to a substantial increase in both absorption and emission processes between the system qubits and the bath. This thermal activation drives the system toward faster decoherence and energy exchange, thereby reducing the effectiveness of QEC in preserving the initial quantum information.

For the collective noise configuration, the elevated temperature amplifies correlated fluctuations in the shared bath, resulting in stronger collective dephasing and dissipation processes. In both the weak and the larger coupling cases, the five-qubit code still yields higher fidelities than the uncorrected evolution, but the relative advantage is smaller than at low temperatures (Fig. 6-7). The fidelity curves for $\kappa = 0.1\omega$ closely track those for $\kappa = 0.01\omega$, indicating that, once the temperature is high, thermal noise rather than the precise value of the coupling strength primarily dictates the dynamics. In direct analogy with the low-temperature limit, Fig. 5(b) characterizes the regime where QEC provides an advantage for entangled states at high temperatures.

On the other hand, for the local noise scenario, where each qubit interacts with an independent high-temperature bath, the five-qubit code does not provide any improvement over the uncorrected evolution. The increased uncorrelated thermal fluctuations lead to strong individual decoherence channels, again limiting the gain achievable by QEC. Overall, in the high-temperature limit, rising thermal noise overwhelms much of the protective capacity of the codes: QEC still slows down fidelity decay, but cannot prevent the eventual approach to a mixed thermal state.

The comparative analysis of different QEC codes across the weak and larger systembath coupling regimes reveals that

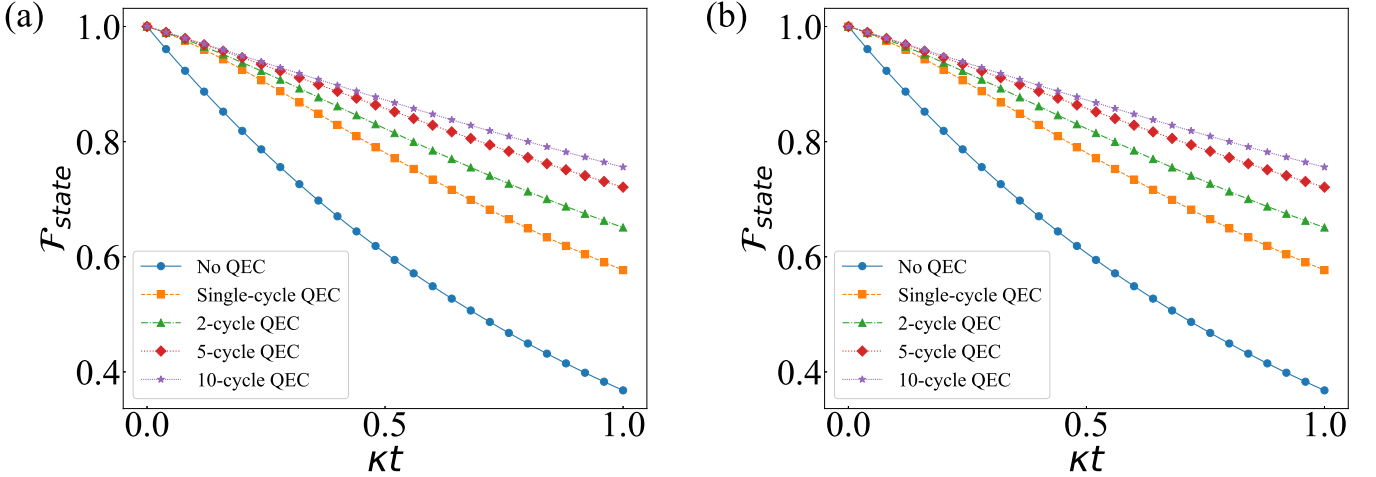


Figure 3. State fidelity $\mathcal{F}_{\text{state}}$ of the initial state $|0\rangle\langle 0|$ as a function of time t and coupling strength κ with and without five-qubit QEC. Single and multiple cycle QEC are considered for the analysis. All qubits are coupled to baths with coupling strength (a) $\kappa/\omega = 0.01$ and (b) $\kappa/\omega = 0.1$, with the bath temperature $T = 0.2$. The fidelity increases with the increase in the number of QEC cycles.

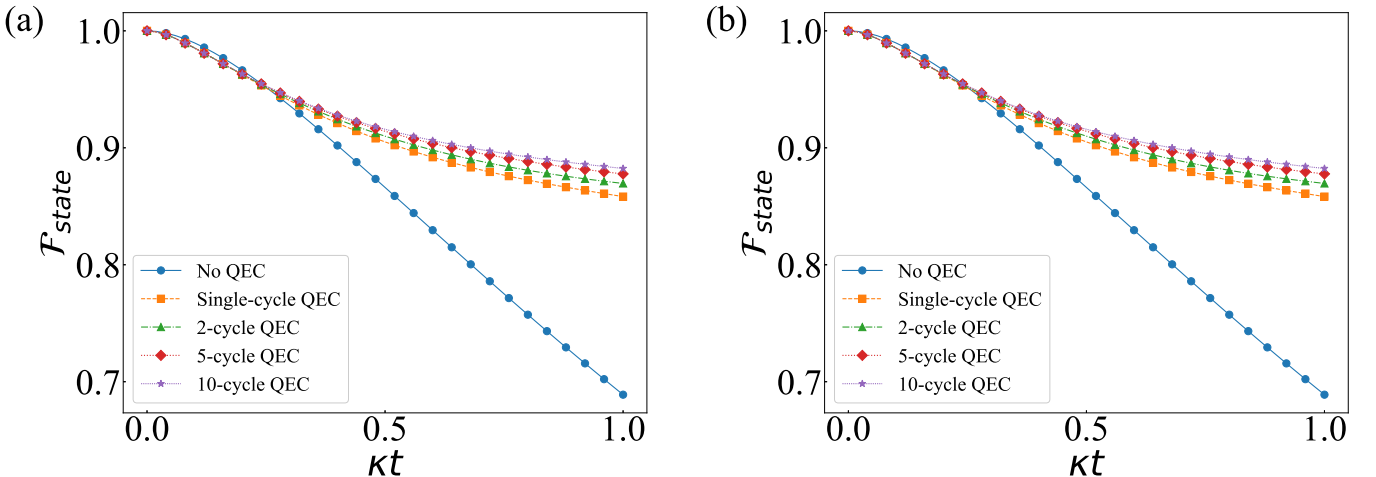


Figure 4. State fidelity $\mathcal{F}_{\text{state}}$ of the initial state $p |\psi^-\rangle\langle\psi^-| + (1 - p) \frac{I}{4}$ for $p = 0.5$ as a function of time t and coupling strength κ with and without five-qubit QEC. We have considered single as well as multiple cycles QEC. In the (a) weak coupling regime, i.e., $\kappa/\omega = 0.01$ and (b) large system-bath coupling regime, i.e., $\kappa/\omega = 0.1$, all the qubits are considered to be coupled to baths with a temperature $T = 0.2$.

the five-qubit code provides a markedly superior performance in preserving the quantum state compared to both the Steane and toric codes. Across both weak and larger system-bath coupling regimes, the five-qubit code consistently achieves higher fidelities than the Steane and toric codes. In Appendix F, we show the performance comparison of the five-qubit code, Steane code and Toric code, taking initial states as $|0\rangle, |1\rangle$ and different Werner states. In the weak-coupling case, this advantage is most pronounced, with the five-qubit code maintaining significantly improved state preservation over multiple QEC cycles. For larger coupling, all codes experience a faster overall decay, but the qualitative behavior of the fidelity curves remains similar to the weak-coupling limit, and the five-qubit code still provides the highest fidelities at each time. This advantage arises from its minimal code size and fully entangled

structure, which enables faster recovery and reduced accumulation of uncorrected errors.

In contrast, the Steane and toric codes, while effective in fault-tolerant and topological architectures, respectively, exhibit slower recovery dynamics and greater sensitivity to environmental perturbations in the same regime. Their larger code spaces and higher overhead make them less efficient in combating weak but frequent noise processes.

V. CONCLUSION

To summarize, we have presented a systematic investigation of the *resilience* of quantum information in OQSs subjected to realistic environmental interactions. By explic-

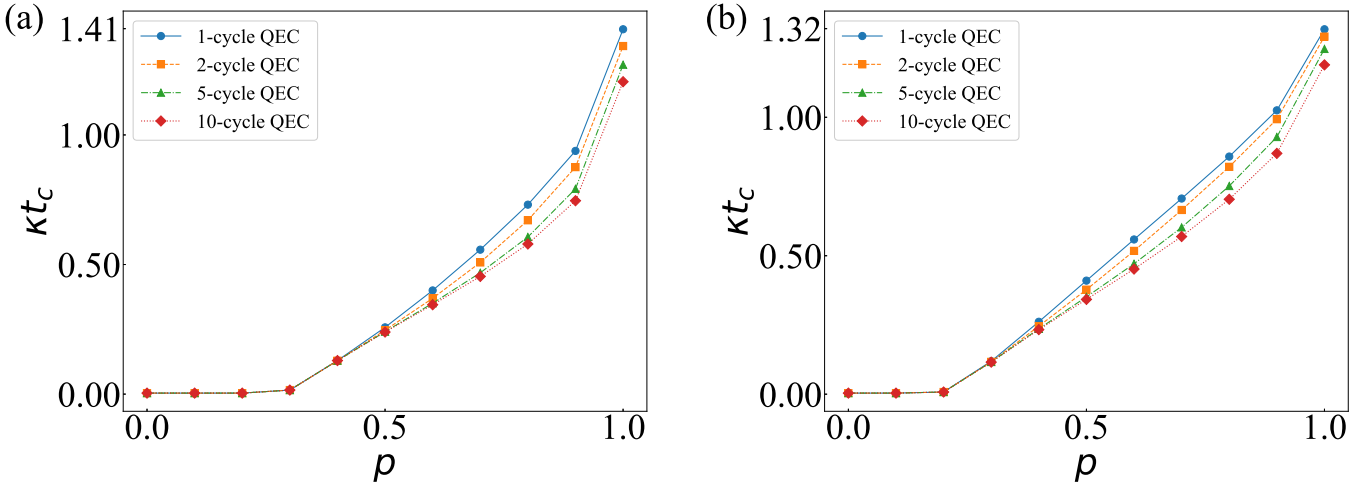


Figure 5. The critical values κt_c where QEC fails to improve fidelity are plotted against mixing parameter p of different Werner states $p|\psi^-\rangle\langle\psi^-| + (1-p)\frac{I}{4}$. Single and multiple cycle five-qubit QEC are considered for the process. All qubits are coupled to baths with coupling strength $\kappa/\omega = 0.01$, with the bath temperature a) $T = 0.2$ and (b) $T = 10$. This indicates that this five-qubit QEC cannot protect entanglements. However, the critical value can be reduced by multiple cycles of QEC.

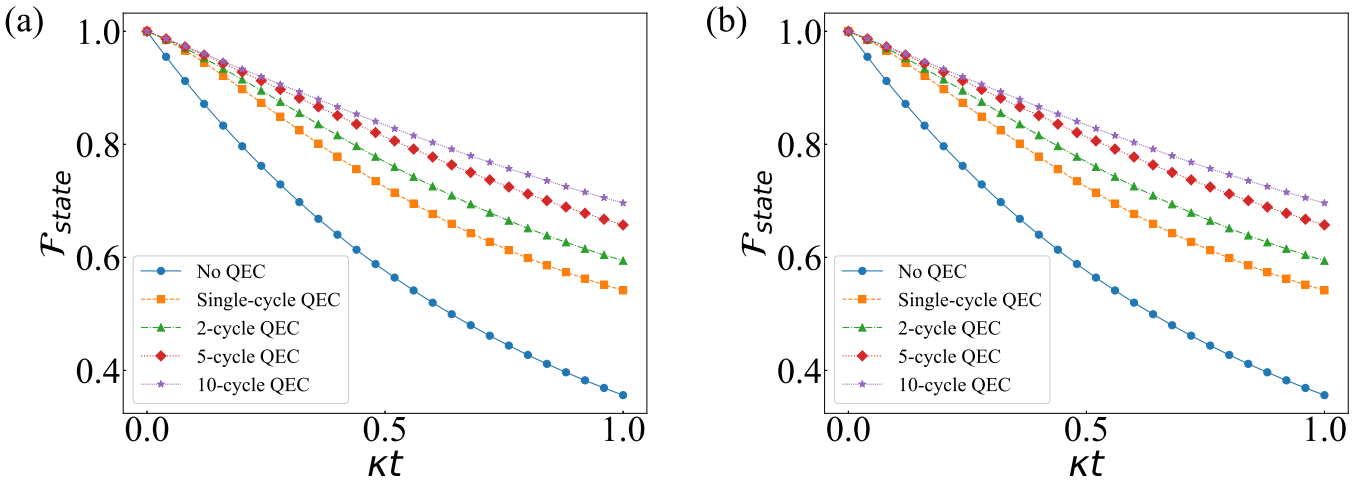


Figure 6. Same as Fig. 3 with bath temperature $T = 10$. The fidelity curves depict the same qualitative improvement with increasing QEC cycles as in the low-temperature case.

itly modeling the systembath coupling within a microscopic Hamiltonian framework and analyzing the resulting dynamics through the master equation formalism, we have quantitatively assessed the performance of several leading QEC codes, namely, the five-qubit, Steane, and toric codes, across different regimes of coupling strength and bath temperatures. This approach goes beyond conventional channel-based analyses by capturing the interplay between decoherence, dissipation, and non-Markovian effects inherent to realistic quantum environments.

Our results show that in the *low-temperature limit*, the five-qubit code provides a significant *enhancement* in preserving quantum state fidelity for both weak and moderately strong systembath coupling. Multiple QEC cycles further suppress decoherence, demonstrating that repetitive correction effec-

tively counteracts the cumulative effects of environmental noise within this coupling range. For two-qubit entangled states, a crossover behavior emerges, where QEC protection becomes less efficient as the degree of entanglement increases, indicating that stronger inter-qubit correlations can enhance the susceptibility to environmental decoherence.

In the *high-temperature regime*, thermal excitations in the bath considerably *degrade* the performance of all QEC codes. The enhanced population of excited bosonic modes increases both emission and absorption processes, accelerating decoherence and energy relaxation. As a result, the relative advantage of QEC is reduced compared with the low-temperature case, and the system approaches thermal equilibrium more rapidly. Nevertheless, the five-qubit code remains the most robust among the codes examined, maintaining higher fidelities

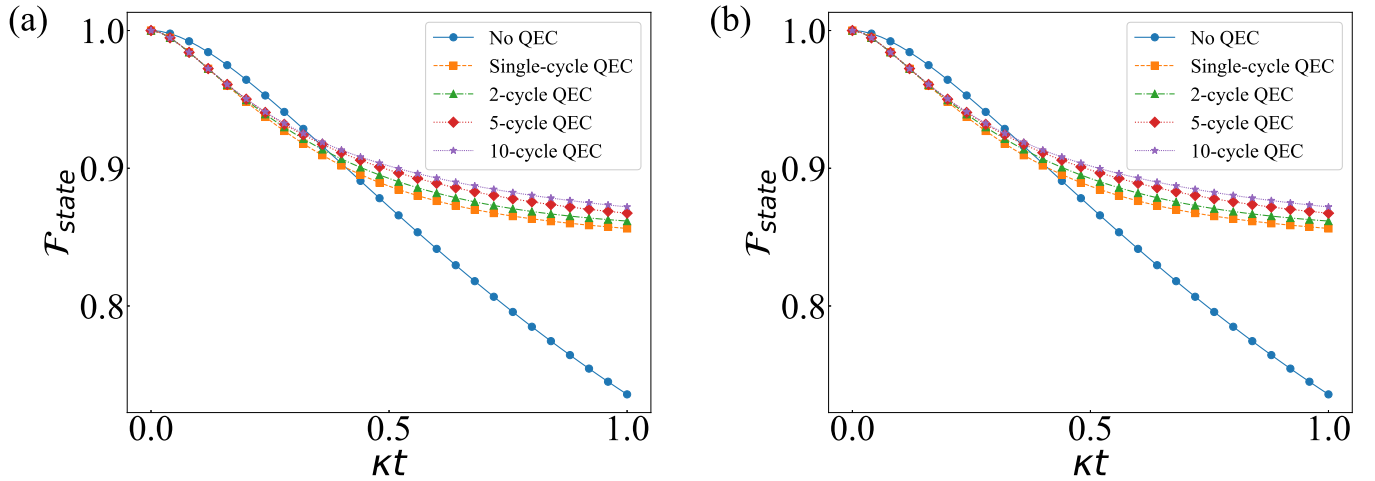


Figure 7. Same as Fig. 4 with bath temperature $T = 10$. The fidelity curves depict the same qualitative improvement with increasing QEC cycles as in the low-temperature case.

than the Steane and toric codes over the full range of coupling strengths considered.

Taken together, these findings underline that compact QEC architectures, such as the five-qubit code, are better suited compared to the CSS code for near-term quantum devices operating in open-system conditions, where resources are constrained and noise correlations are significant. Moreover, they reveal the limitations of conventional QEC codes when faced with high thermal noise and larger systembath coupling, highlighting the need for modified or adaptive correction strategies that account for the underlying physical noise structure.

Building on these results, several promising research directions emerge. First, it would be valuable to extend this framework to the *surface code* and *dynamical QEC schemes* that adapt correction intervals or code parameters based on the evolving decoherence rates inferred from the environment. Second, investigating *hybrid QEC strategies* that integrate bosonic or continuous-variable encodings with discrete stabilizer codes may offer improved protection in regimes dominated by thermal and dissipative noise. Finally, exploring

the thermodynamic cost and entropy production associated with QEC operations in open systems could establish a deeper connection between information recovery, dissipation, and the fundamental limits of reversibility in quantum dynamics. Such extensions would not only advance the theoretical understanding of QEC in realistic environments but also provide *practical guidelines for implementing noise-resilient quantum computation and communication protocols* in the next generation of quantum devices.

VI. ACKNOWLEDGEMENT

NB and PC would like to thank Saikat Sur of the Indian Institute of Mathematical Science, Chennai, and Avijit Misra of the Indian Institute of Technology, Dhanbad, for their valuable inputs and suggestions. P.C. acknowledges the support from the International Postdoctoral Fellowship from the Ben May Center for Theory and Computation.

[1] Lov K. Grover, “A fast quantum mechanical algorithm for database search,” in *Proceedings of the Twenty-Eighth Annual ACM Symposium on Theory of Computing*, STOC ’96 (Association for Computing Machinery, New York, NY, USA, 1996) p. 212219.

[2] Peter W Shor, “Polynomial-time algorithms for prime factorization and discrete logarithms on a quantum computer,” *SIAM review* **41**, 303–332 (1999).

[3] Sanjeev Arora and Boaz Barak, *Computational complexity: a modern approach* (Cambridge University Press, 2009).

[4] Michael A Nielsen and Isaac L Chuang, *Quantum computation and quantum information: 10th Anniversary Edition* (Cambridge University Press, 2010).

[5] Valentin Gebhart, Luca Pezzè, and Augusto Smerzi, “Quantifying computational advantage of grovers algorithm with the trace speed,” *Scientific Reports* **11**, 1288 (2021).

[6] Frank Arute, Kunal Arya, Ryan Babbush, Dave Bacon, Joseph C Bardin, Rami Barends, Rupak Biswas, Sergio Boixo, Fernando GSL Brandao, David A Buell, *et al.*, “Quantum supremacy using a programmable superconducting processor,” *Nature* **574**, 505–510 (2019).

[7] Han-Sen Zhong, Yu-Hao Deng, Jian Qin, Hui Wang, Ming-Cheng Chen, Li-Chao Peng, Yi-Han Luo, Dian Wu, Si-Qiu Gong, Hao Su, *et al.*, “Phase-programmable gaussian boson sampling using stimulated squeezed light,” *Physical review letters* **127**, 180502 (2021).

[8] Emanuel Knill, “Quantum computing with realistically noisy devices,” *Nature* **434**, 39–44 (2005).

[9] John Preskill, “Quantum computing in the nisq era and beyond,” *Quantum* **2**, 79 (2018).

[10] Konstantinos Georgopoulos, Clive Emery, and Paolo Zuliani, “Modeling and simulating the noisy behavior of near-term quantum computers,” *Physical Review A* **104**, 062432 (2021).

[11] Xu-Dan Xie, Xiaoming Zhang, Balint Koczor, and Xiao Yuan, “Advances in quantum computation in nisq era,” *Entropy* **27** (2025), 10.3390/e27101074.

[12] Peter W Shor, “Scheme for reducing decoherence in quantum computer memory,” *Physical review A* **52**, R2493 (1995).

[13] A. M. Steane, “Error correcting codes in quantum theory,” *Phys. Rev. Lett.* **77**, 793–797 (1996).

[14] Daniel Gottesman, “Class of quantum error-correcting codes saturating the quantum hamming bound,” *Phys. Rev. A* **54**, 1862–1868 (1996).

[15] Raymond Laflamme, Cesar Miquel, Juan Pablo Paz, and Wojciech Hubert Zurek, “Perfect quantum error correcting code,” *Physical Review Letters* **77**, 198 (1996).

[16] A. R. Calderbank and Peter W. Shor, “Good quantum error-correcting codes exist,” *Phys. Rev. A* **54**, 1098–1105 (1996).

[17] Andrew Steane, “Multiple-particle interference and quantum error correction,” *Proceedings of the Royal Society of London. Series A: Mathematical, Physical and Engineering Sciences* **452**, 2551–2577 (1996).

[18] Charles H. Bennett, David P. DiVincenzo, John A. Smolin, and William K. Wootters, “Mixed-state entanglement and quantum error correction,” *Phys. Rev. A* **54**, 3824–3851 (1996).

[19] Emanuel Knill and Raymond Laflamme, “Theory of quantum error-correcting codes,” *Physical Review A* **55**, 900 (1997).

[20] Daniel Gottesman, *Stabilizer codes and quantum error correction*, Ph.D. thesis, California Institute of Technology (1997).

[21] Isaac L Chuang, Debbie W Leung, and Yoshihisa Yamamoto, “Bosonic quantum codes for amplitude damping,” *Physical Review A* **56**, 1114 (1997).

[22] A. R. Calderbank, E. M. Rains, P. W. Shor, and N. J. A. Sloane, “Quantum error correction and orthogonal geometry,” *Phys. Rev. Lett.* **78**, 405–408 (1997).

[23] Emanuel Knill, Raymond Laflamme, and Wojciech H. Zurek, “Resilient quantum computation: Error models and thresholds,” *Proceedings of the Royal Society A: Mathematical, Physical and Engineering Sciences* **454**, 365–384 (1998).

[24] David G Cory, MD Price, W Maas, Emanuel Knill, Raymond Laflamme, Wojciech H Zurek, Timothy F Havel, and Shyamal S Somaroo, “Experimental quantum error correction,” *Physical Review Letters* **81**, 2152 (1998).

[25] Samuel L Braunstein, “Quantum error correction for communication with linear optics,” *Nature* **394**, 47–49 (1998).

[26] P. T. Cochrane, G. J. Milburn, and W. J. Munro, “Macroscopically distinct quantum-superposition states as a bosonic code for amplitude damping,” *Phys. Rev. A* **59**, 2631–2634 (1999).

[27] John Chiaverini, Dietrich Leibfried, Tobias Schaetz, Murray D Barrett, RB Blakestad, Joseph Britton, Wayne M Itano, John D Jost, Emanuel Knill, Christopher Langer, *et al.*, “Realization of quantum error correction,” *Nature* **432**, 602–605 (2004).

[28] David W. Kribs, Raymond Laflamme, David Poulin, and Maia Lesosky, “Operator quantum error correction,” *Quantum Information & Computation* **6**, 382–399 (2006).

[29] David Kribs, Raymond Laflamme, and David Poulin, “Unified and generalized approach to quantum error correction,” *Physical review letters* **94**, 180501 (2005).

[30] Panos Aliferis, Daniel Gottesman, and John Preskill, “Quantum accuracy threshold for concatenated distance-3 codes,” *Quantum Info. Comput.* **6**, 97165 (2006).

[31] TB Pittman, BC Jacobs, and JD Franson, “Demonstration of quantum error correction using linear optics,” *Physical Review A* **71**, 052332 (2005).

[32] Ognyan Oreshkov and Todd A Brun, “Continuous quantum error correction for non-markovian decoherence,” *Physical Review A* **76**, 022318 (2007).

[33] Panos Aliferis, Daniel Gottesman, and John Preskill, “Accuracy threshold for postselected quantum computation,” *Quantum Info. Comput.* **8**, 181244 (2008).

[34] Austin G Fowler, Ashley M Stephens, and Peter Groszkowski, “High-threshold universal quantum computation on the surface code,” *Physical Review A* **80**, 052312 (2009).

[35] Hui Khoon Ng and Prabha Mandayam, “Simple approach to approximate quantum error correction based on the transpose channel,” *Physical Review A* **81**, 062342 (2010).

[36] Austin G Fowler, “Two-dimensional color-code quantum computation,” *Physical Review A* **83**, 042310 (2011).

[37] Philipp Schindler, Julio T. Barreiro, Thomas Monz, Volckmar Nebendahl, Daniel Nigg, Michael Chwalla, Markus Hennrich, and Rainer Blatt, “Experimental repetitive quantum error correction,” *Science* **332**, 1059–1061 (2011).

[38] David S Wang, Austin G Fowler, and Lloyd CL Hollenberg, “Surface code quantum computing with error rates over 1%,” *Physical Review A* **83**, 020302 (2011).

[39] Prabha Mandayam and Hui Khoon Ng, “Towards a unified framework for approximate quantum error correction,” *Physical Review A* **86**, 012335 (2012).

[40] Austin G Fowler, Matteo Mariantoni, John M Martinis, and Andrew N Cleland, “Surface codes: Towards practical large-scale quantum computation,” *Physical Review A* **86**, 032324 (2012).

[41] Matthew D Reed, Leonardo DiCarlo, Simon E Nigg, Luyan Sun, Luigi Frunzio, Steven M Girvin, and Robert J Schoelkopf, “Realization of three-qubit quantum error correction with superconducting circuits,” *Nature* **482**, 382–385 (2012).

[42] Xing-Can Yao, Tian-Xiong Wang, Hao-Ze Chen, Wei-Bo Gao, Austin G Fowler, Robert Raussendorf, Zeng-Bing Chen, Nai-Le Liu, Chao-Yang Lu, You-Jin Deng, *et al.*, “Experimental demonstration of topological error correction,” *Nature* **482**, 489–494 (2012).

[43] Daniel A Lidar and Todd A Brun, eds., *Quantum error correction* (Cambridge University Press, 2013).

[44] Joel J Wallman, “Bounding experimental quantum error rates relative to fault-tolerant thresholds,” *arXiv preprint arXiv:1511.00727* (2015), 10.48550/arXiv.1511.00727.

[45] Ben Criger and Barbara Terhal, “Noise thresholds for the [4,2,2]-concatenated toric code,” *Quantum Info. Comput.* **16**, 12611281 (2016).

[46] Marios H Michael, Matti Silveri, RT Brierley, Victor V Albert, Juha Salmilehto, Liang Jiang, and Steven M Girvin, “New class of quantum error-correcting codes for a bosonic mode,” *Physical Review X* **6**, 031006 (2016).

[47] Nissim Ofek, Andrei Petrenko, Reinier Heeres, Philip Reinhold, Zaki Leghtas, Brian Vlastakis, Yehan Liu, Luigi Frunzio, SM Girvin, Liang Jiang, *et al.*, “Extending the lifetime of a quantum bit with error correction in superconducting circuits,” *Nature* **536**, 441–445 (2016).

[48] Wei-Yue Liu, Xian-Feng Zhong, Teng Wu, Feng-Zhi Li, Biao Jin, Yu Tang, Heng-Ming Hu, Zheng-Ping Li, Liang Zhang, Wen-Qi Cai, *et al.*, “Experimental free-space quantum key distribution with efficient error correction,” *Optics Express* **25**, 10716–10723 (2017).

[49] Yink Loong Len and Hui Khoon Ng, “Open-system quantum error correction,” *Phys. Rev. A* **98**, 022307 (2018).

[50] Giuliano Gadioli La Guardia, *Quantum Error Correction: Symmetric, Asymmetric, Synchronizable, and Convolutional Codes*, 1st ed., Quantum Science and Technology (Springer Cham,

2020) pp. XIII, 227.

[51] C Ryan-Anderson, NC Brown, MS Allman, B Arkin, G Asa-Attua, C Baldwin, J Berg, JG Bohnet, S Braxton, N Burdick, *et al.*, “Implementing fault-tolerant entangling gates on the five-qubit code and the color code,” *arXiv preprint arXiv:2208.01863* (2022), <https://doi.org/10.48550/arXiv.2208.01863>.

[52] Aravind P. Babu, Tuure Orell, Vasilii Vadimov, Wallace Teixeira, Mikko Möttönen, and Matti Silveri, “Quantum error correction under numerically exact open-quantum-system dynamics,” *Phys. Rev. Res.* **5**, 043161 (2023).

[53] Google Quantum AI, “Suppressing quantum errors by scaling a surface code logical qubit,” *Nature* **614**, 676–681 (2023).

[54] Yoni Choukroun and Lior Wolf, “Deep quantum error correction,” (2023), *arXiv:2301.11930 [quant-ph]*.

[55] Andrew Tanggara, Mile Gu, and Kishor Bharti, “Strategic code: A unified spatio-temporal framework for quantum error-correction,” *arXiv preprint arXiv:2405.17567* (2024), [10.48550/arXiv.2405.17567](https://doi.org/10.48550/arXiv.2405.17567).

[56] Andrew Tanggara, Mile Gu, and Kishor Bharti, “Simple construction of qudit floquet codes on a family of lattices,” *arXiv preprint arXiv:2410.02022* (2024), [10.48550/arXiv.2410.02022](https://doi.org/10.48550/arXiv.2410.02022).

[57] Nirupam Basak, Andrew Tanggara, Ankith Mohan, Goutam Paul, and Kishor Bharti, “Approximate dynamical quantum error-correcting codes,” *arXiv preprint arXiv:2502.09177* (2025), [10.48550/arXiv.2502.09177](https://doi.org/10.48550/arXiv.2502.09177).

[58] Nirupam Basak and Goutam Paul, “Resource reduction in multiparty quantum secret sharing of both classical and quantum information under noisy scenario,” *arXiv preprint arXiv:2504.16709* (2025), [10.48550/arXiv.2504.16709](https://doi.org/10.48550/arXiv.2504.16709).

[59] Nirupam Basak and Goutam Paul, “Multiparty quantum secret sharing of classical message under noisy scenario,” in *2025 IEEE International Conference on Quantum Control, Computing and Learning (qCCL)* (IEEE, Hong Kong, 2025) pp. 143–148.

[60] Daniel J Spencer, Andrew Tanggara, Tobias Haug, Derek Khu, and Kishor Bharti, “Qudit low-density parity-check codes,” *arXiv preprint arXiv:2510.06495* (2025), [10.48550/arXiv.2510.06495](https://doi.org/10.48550/arXiv.2510.06495).

[61] Esther Xiaozhen Fu and Daniel Gottesman, “Error Correction in Dynamical Codes,” *Quantum* **9**, 1886 (2025).

[62] D. Aharonov and M. Ben-Or, “Fault-tolerant quantum computation with constant error,” in *Proceedings of the Twenty-Ninth Annual ACM Symposium on Theory of Computing*, STOC ’97 (Association for Computing Machinery, New York, NY, USA, 1997) p. 176188.

[63] A.Yu. Kitaev, “Fault-tolerant quantum computation by anyons,” *Annals of Physics* **303**, 2–30 (2003).

[64] Andrew M Steane, “Overhead and noise threshold of fault-tolerant quantum error correction,” *Physical Review A* **68**, 042322 (2003).

[65] Barbara M Terhal and Guido Burkard, “Fault-tolerant quantum computation for local non-markovian noise,” *Physical Review A* **71**, 012336 (2005).

[66] Dorit Aharonov, Alexei Kitaev, and John Preskill, “Fault-tolerant quantum computation with long-range correlated noise,” *Physical review letters* **96**, 050504 (2006).

[67] Robert Raussendorf and Jim Harrington, “Fault-tolerant quantum computation with high threshold in two dimensions,” *Physical review letters* **98**, 190504 (2007).

[68] Dorit Aharonov and Michael Ben-Or, “Fault-tolerant quantum computation with constant error rate,” *SIAM Journal on Computing* **38**, 1207–1282 (2008).

[69] Hui Khoon Ng and John Preskill, “Fault-tolerant quantum computation versus gaussian noise,” *Physical Review A* **79**, 032318 (2009).

[70] Ashley M Stephens, “Fault-tolerant thresholds for quantum error correction with the surface code,” *Physical Review A* **89**, 022321 (2014).

[71] Timo Hillmann, Guillaume Dauphinais, Ilan Tzitrin, and Michael Vasmer, “Single-shot and measurement-based quantum error correction via fault complexes,” *Phys. Rev. A* **112**, L040401 (2025).

[72] Alicja Dutkiewicz, Stefano Polla, Maximilian Scheurer, Christian Gogolin, William J. Huggins, and Thomas E. O’Brien, “Error mitigation and circuit division for early fault-tolerant quantum phase estimation,” *PRX Quantum* **6**, 040318 (2025).

[73] Yutaro Akahoshi, Riki Toshio, Jun Fujisaki, Hirotaka Oshima, Shintaro Sato, and Keisuke Fujii, “Compilation of trotter-based time evolution for partially fault-tolerant quantum computing architecture,” *PRX Quantum* **6**, 040319 (2025).

[74] Asher Peres, “Reversible logic and quantum computers,” *Physical review A* **32**, 3266 (1985).

[75] A Yu Kitaev, “Quantum codes on a lattice with boundary,” *arXiv preprint quant-ph/9811052* (1998), [10.48550/arXiv.quant-ph/9811052](https://doi.org/10.48550/arXiv.quant-ph/9811052).

[76] Daniel A. Lidar and Todd A. Brun, “Introduction to decoherence and noise in open quantum systems,” in *Quantum Error Correction*, edited by Daniel A. Lidar and Todd A. Brun (Cambridge University Press, 2013) p. 345.

[77] Pritam Chattopadhyay and Goutam Paul, “Understanding the thermodynamics of computation: a pedagogical overview: P. chattopadhyay, g. paul,” *Quantum Information Processing* **24**, 305 (2025).

[78] Alexander Erhard, Hendrik Poulsen Nautrup, Michael Meth, Lukas Postler, Roman Stricker, Martin Stadler, Vlad Negnevitsky, Martin Ringbauer, Philipp Schindler, Hans J Briegel, *et al.*, “Entangling logical qubits with lattice surgery,” *Nature* **589**, 220–224 (2021).

[79] Pritam Chattopadhyay, Avijit Misra, Tanmoy Pandit, and Goutam Paul, “Landauer principle and thermodynamics of computation,” *Reports on Progress in Physics* **88**, 086001 (2025).

[80] Heinz-Peter Breuer and Francesco Petruccione, *The Theory of Open Quantum Systems* (Oxford University Press, 2007).

[81] Herbert Spohn, “Entropy production for quantum dynamical semigroups,” *Journal of Mathematical Physics* **19**, 1227–1230 (1978).

[82] C. Lindblad, *Non-Equilibrium Entropy and Irreversibility*, Mathematical Physics Studies, Vol. 5 (Springer Dordrecht, Dordrecht, Holland, 2001) pp. X, 166.

[83] Maximilian Schlosshauer, *Decoherence and the Quantum-to-Classical Transition*, 1st ed. (Springer Berlin, Heidelberg, 2007) pp. xv, 416.

[84] Wojciech Hubert Zurek, “Quantum darwinism,” *Nature physics* **5**, 181–188 (2009).

[85] Christopher Jarzynski, “Equalities and inequalities: Irreversibility and the second law of thermodynamics at the nanoscale,” *Annu. Rev. Condens. Matter Phys.* **2**, 329–351 (2011).

[86] Erich Joos, H. Dieter Zeh, Claus Kiefer, Domenico Giulini, Joachim Kupsch, and Ion-Olimpiu Stamatescu, *Decoherence and the Appearance of a Classical World in Quantum Theory*, 2nd ed. (Springer Berlin, Heidelberg, 2013) pp. XII, 496.

[87] TB Batalhão, AM Souza, RS Sarthour, IS Oliveira, M Paternostro, E Lutz, and RM Serra, “Irreversibility and the arrow of time in a quenched quantum system,” *Physical review letters* **115**, 190601 (2015).

- [88] Andrew Steane, “Quantum computing,” *Reports on Progress in Physics* **61**, 117 (1998).
- [89] Ilan Kremer, *Quantum communication*, Master’s thesis, Hebrew University of Jerusalem (1995).
- [90] Khabat Heshami, Duncan G. England, Peter C. Humphreys, Philip J. Bustard, Victor M. Acosta, Joshua Nunn, and Benjamin J. Sussman, “Quantum memories: emerging applications and recent advances,” *Journal of Modern Optics* **63**, 2005–2028 (2016).
- [91] Pritam Chattopadhyay, “Non-gaussian dissipative quantum thermometry beyond gaussian bounds,” *Phys. Rev. A* **112**, 062606 (2025).
- [92] Luis A. Correa, Mohammad Mehboudi, Gerardo Adesso, and Anna Sanpera, “Individual quantum probes for optimal thermometry,” *Physical Review Letters* **114**, 220405 (2015).
- [93] Mohammad Mehboudi, Anna Sanpera, Juan M. R. Parrondo, and Luis A. Correa, “Thermometry in the quantum regime: Recent theoretical progress,” *Journal of Physics A: Mathematical and Theoretical* **52**, 303001 (2019).
- [94] Patrick P. Potts, Jonatan Bohr Brask, and Nicolas Brunner, “Fundamental limits on low-temperature quantum thermometry with finite resolution,” *Quantum* **3**, 161 (2019).
- [95] Vittorio Vitale, Aniket Rath, Petar Jurcevic, Andreas Elben, Cyril Branciard, and Benoît Vermersch, “Robust estimation of the quantum fisher information on a quantum processor,” *PRX Quantum* **5**, 030338 (2024).
- [96] Angel Rivas and Susana F Huelga, *Open quantum systems*, Vol. 10 (Springer, 2012).
- [97] Richard Jozsa, “Fidelity for mixed quantum states,” *Journal of Modern Optics* **41**, 2315–2323 (1994).

Appendix A: Bath Response functions

Using the standard definition of the bath correlation functions, which encapsulate the response of the thermal reservoir to the system-bath coupling, we write:

$$\Phi_{\alpha\alpha'}(\tau) = \text{Tr}_B(B_\alpha(\tau)B_{\alpha'}(0)\rho_B),$$

where ρ_B denotes the thermal state of the bath, and $B_{\alpha,j}$ represents the interaction-picture time evolution of the bath operators under the free bath Hamiltonian H_B . Using this definition and expanding the operator $B_{\alpha,j}$ in terms of the bosonic creation and annihilation operators, the two-point bath correlation function can be explicitly evaluated as:

$$\begin{aligned} \Phi_{\alpha\alpha'}(\tau) &= \langle B_{\alpha,j}(t-\tau)B_{\alpha',j}(t) \rangle_B \\ &= \text{tr}\{B_{\alpha,j}(t-\tau)B_{\alpha',j}(t)\rho_B\} \\ &= \text{tr}\left(e^{iH_B(t-\tau)}B_{\alpha,j}e^{-iH_B(t-\tau)}e^{iH_B t}B_{\alpha',j}e^{-iH_B t}\rho_B\right) \\ &= \text{tr}\left(e^{-iH_B\tau}B_{\alpha,j}e^{iH_B\tau}B_{\alpha',j}\rho_B\right) \\ &= \sum_{kk'}(g_{k,j}g_{k',j}\Gamma(\tau; k, k')) \end{aligned} \quad (\text{A1})$$

where the kernel $\Gamma(\tau; k, k')$ encodes the dynamical contributions of the bath modes and depends on the indices α, α' as follows:

$$\Gamma(\tau; k, k') = \begin{cases} e^{i\tau\Omega_{k,j}}\langle b_{k,j}b_{k',j}^\dagger \rangle_B & \alpha = \alpha' = 1 \\ e^{i\tau\Omega_{k,j}}\langle b_{k,j}b_{k',j}^\dagger \rangle_B & \alpha = 1, \alpha' = 2 \\ e^{-i\tau\Omega_{k,j}}\langle b_{k,j}^\dagger b_{k',j} \rangle_B & \alpha = 2, \alpha' = 1 \\ e^{-i\tau\Omega_{k,j}}\langle b_{k,j}^\dagger b_{k',j} \rangle_B & \alpha = \alpha' = 2 \end{cases} \quad (\text{A2})$$

$$= \begin{cases} 0 & \alpha = \alpha' \\ \delta_{kk'}e^{i\Omega_{k,j}\tau}(n_j(\omega_j) + 1) & \alpha = 1, \alpha' = 2 \\ \delta_{kk'}e^{-i\Omega_{k,j}\tau}(n_j(\omega_j)) & \alpha = 2, \alpha' = 1 \end{cases} \quad (\text{A3})$$

where $n_j(\Omega) = \frac{1}{e^{\frac{\Omega}{k_B T_j}} - 1}$, k_B is Boltzmann constant, T_j is the temperature of j -th bath. Therefore, substituting these thermal averages yields the simplified form:

$$\Phi_{\alpha\alpha'}(\tau) = \begin{cases} 0, & \alpha = \alpha' \\ \sum_k |g_{k,j}|^2 e^{i\Omega_{k,j}\tau} (n_j(\omega_j) + 1), & \alpha = 1, \alpha' = 2 \\ \sum_k |g_{k,j}|^2 e^{-i\Omega_{k,j}\tau} (n_j(\omega_j)), & \alpha = 2, \alpha' = 1 \end{cases} \quad (\text{A4})$$

with $\sum_k |g_{k,j}|^2$, is a finite positive number dependent on the nature of interaction between the bath and the system qubits. These correlation functions serve as the fundamental inputs for characterizing both dissipative and decoherence dynamics in open quantum systems.

Appendix B: Solution to the Master equation

The time-nonlocal master equation, commonly referred to as the Nakajima-Zwanzig master equation [80], governs the evolution of the reduced density operator $\rho_S(t)$ of the system. To second order in the system-bath coupling strength, this equation encapsulates the non-Markovian dynamics arising from the system's interaction with its environment, and is expressed as:

$$\begin{aligned}
\dot{\rho}_S(t) &= -i[H_S(t), \rho_S(t)] + \int_{s=0}^t ds \operatorname{tr}_B \{ [H_{SB}(t)\rho_S(t)\rho_B, H_{SB}(t-s)] \} + h.c. \\
&= -i[H_S(t), \rho_S(t)] + \int_{s=0}^t ds \operatorname{tr}_B \{ H_{SB}(t)\rho_S(t)\rho_B H_{SB}(t-s) - H_{SB}(t-s)H_{SB}(t)\rho_S(t)\rho_B \} + h.c. \\
&= -i[H_S(t), \rho_S(t)] + \left[S_1(t)\rho_S(t) \left(\int_0^t ds S_2(t-s)\Phi_{21}(-s) \right) + S_2(t)\rho_S(t) \left(\int_0^t ds S_1(t-s)\Phi_{12}(-s) \right) \right. \\
&\quad \left. - \left(\int_0^t ds \Phi_{12}(-s)S_1(t-s) \right) S_2(t)\rho_S(t) - \left(\int_0^t ds \Phi_{21}(-s)S_2(t-s) \right) S_1(t)\rho_S(t) \right] + h.c. \\
&= -i[H_S(t), \rho_S(t)] + \left[S_1(t)\rho_S(t)W_2(t) + S_2(t)\rho_S(t)W_1(t) - W_1(t)S_2(t)\rho_S(t) - W_2(t)S_1(t)\rho_S(t) \right] + h.c.
\end{aligned} \tag{B1}$$

where the operators $W_1(t)$ and $W_2(t)$ encapsulate the bath-induced memory effects and are defined as:

$$\begin{aligned}
W_1(t) &= \int_0^t ds S_1(t-s)\Phi_{12}(-s), \\
W_2(t) &= \int_0^t ds S_2(t-s)\Phi_{21}(-s),
\end{aligned} \tag{B2}$$

where, $S(t)$ are given in Eq. (8). The bath correlation functions $\phi_{ij}(-s)$ encapsulate the statistical properties of the environment and mediate the non-Markovian features of the dynamics.

Master equation for two-qubit logical system QEC

The $S_{1(2),j}$ operator as defined in Eq. (8) for this case becomes

$$\begin{aligned}
S_{1(2),j}(t) &= e^{iH_S t} S_{1(2),j} e^{-iH_S t} \\
&= e^{-it\frac{\omega_j}{2}\sigma_{zj}} \sigma_j^{+(-)} e^{it\frac{\omega_j}{2}\sigma_{zj}} \\
&= [\cos t\omega_j - (+)i \sin t\omega_j] \sigma_j^{+(-)}
\end{aligned} \tag{B3}$$

Now

$$\begin{aligned}
&\int_0^t d\tau \operatorname{tr}_B [H_j^I(t)\rho_S(t) \otimes \rho_B, H_j^I(t-\tau)] \\
&= \int_0^t d\tau \sum_{\alpha\alpha'} [S_{\alpha,j}(t)\rho_S(t), S_{\alpha',j}(t-\tau)] \langle B_{\alpha',j}(t-\tau)B_{\alpha,j}(t)\rho_B \rangle_B \\
&= \sum_k |g_{k,j}|^2 \left((\sigma_j^+ \rho_S(t) \sigma_j^- - \sigma_j^- \sigma_j^+ \rho_S(t)) \frac{in_j(\omega_j)}{\omega_j + \Omega_{k,j}} (e^{-it(\omega_j + \Omega_{k,j})} - 1) \right. \\
&\quad \left. + (\sigma_j^- \rho_S(t) \sigma_j^+ - \sigma_j^+ \sigma_j^- \rho_S(t)) \frac{-i(n_j(\omega_j) + 1)}{\omega_j + \Omega_{k,j}} (e^{it(\omega_j + \Omega_{k,j})} - 1) \right)
\end{aligned} \tag{B4}$$

Appendix C: Encoding and decoding of five-qubit code

In five-qubit code [15], the encoding operation U encodes one physical qubit into the logical space spanned by $\{|0_L\rangle, |1_L\rangle\}$ using five physical qubits, where

$$\begin{aligned} |0_L\rangle &= U|00000\rangle = \frac{1}{2\sqrt{2}}(-|00000\rangle + |00110\rangle + |01001\rangle + |01111\rangle - |10011\rangle + |10101\rangle + |11010\rangle + |11100\rangle) \\ |1_L\rangle &= U|00100\rangle = \frac{1}{2\sqrt{2}}(-|11111\rangle + |11001\rangle + |10110\rangle + |10000\rangle + |01100\rangle - |01010\rangle - |00101\rangle - |00011\rangle). \end{aligned} \quad (\text{C1})$$

Therefore, for any single qubit density matrix ρ , we can write the encoding as

$$\rho_L = \mathcal{E}(\rho) = U|00\rangle\langle 00| \otimes \rho \otimes |00\rangle\langle 00|U^\dagger. \quad (\text{C2})$$

The state recovery stage consists of decoding, error detection, and correction. The decoding operation is the reverse of the encoding operation. That is, after decoding, we get,

$$\hat{\rho} = \mathcal{D}(\hat{\rho}_L) = U^\dagger \hat{\rho}_L U, \quad (\text{C3})$$

where $\hat{\rho}_L$ is the erroneous state.

The error detection consists of measuring the auxiliary qubits $j = 1, 2, 4, 5$. This measurement is called *syndrome measurement*. Depending on these measurement results, called *error syndrome*, Pauli operations are applied to the main qubit ($j = 3$) to correct the error. We can combine these detections and corrections and write the operation in terms of the Kraus map as

$$|00\rangle\langle 00| \otimes \rho' \otimes |00\rangle\langle 00| = \mathcal{R}(\hat{\rho}) = \sum_{k=0}^{15} R_k \hat{\rho} R_k^\dagger, \quad (\text{C4})$$

where the operators $\{R_k\}$ are given by Ref. [52] as,

$$\begin{aligned} R_0 &= |00\rangle\langle 00| \otimes \sigma_0 \otimes |00\rangle\langle 00|, & R_1 &= |00\rangle\langle 00| \otimes \sigma_z \otimes |00\rangle\langle 01|, \\ R_2 &= |00\rangle\langle 00| \otimes \sigma_0 \otimes |00\rangle\langle 10|, & R_3 &= |00\rangle\langle 00| \otimes \sigma_0 \otimes |00\rangle\langle 11|, \\ R_4 &= |00\rangle\langle 01| \otimes \sigma_0 \otimes |00\rangle\langle 00|, & R_5 &= |00\rangle\langle 01| \otimes \sigma_z \otimes |00\rangle\langle 01|, \\ R_6 &= |00\rangle\langle 01| \otimes \sigma_x \otimes |00\rangle\langle 10|, & R_7 &= |00\rangle\langle 01| \otimes \sigma_x \otimes |00\rangle\langle 11|, \\ R_8 &= |00\rangle\langle 10| \otimes \sigma_0 \otimes |00\rangle\langle 00|, & R_9 &= |00\rangle\langle 10| \otimes \sigma_x \otimes |00\rangle\langle 01|, \\ R_{10} &= |00\rangle\langle 10| \otimes \sigma_z \otimes |00\rangle\langle 10|, & R_{11} &= |00\rangle\langle 10| \otimes \sigma_x \otimes |00\rangle\langle 11|, \\ R_{12} &= |00\rangle\langle 11| \otimes \sigma_z \otimes |00\rangle\langle 00|, & R_{13} &= |00\rangle\langle 11| \otimes \sigma_x \sigma_z \otimes |00\rangle\langle 01|, \\ R_{14} &= |00\rangle\langle 11| \otimes \sigma_x \otimes |00\rangle\langle 10|, & R_{15} &= |00\rangle\langle 11| \otimes \sigma_z \otimes |00\rangle\langle 11|, \end{aligned}$$

where σ_0 is the identity operator and σ_x, σ_z are Pauli operators.

Appendix D: Encoding and decoding of CSS code: Steane Code

Steane code [13, 17] is a seven-qubit stabilizer code that uses the stabilizer formalism. A quantum error correcting code (QECC) with a stabilizer group, which stabilizes the logical codewords, is called a stabilizer code. Each stabilizer code has a set of stabilizer generators that can generate the whole stabilizer group. From this information, one can easily derive the logical codewords and logical operations. The error syndromes are given by the measurement of stabilizer generators. The six stabilizer generators of the Steane code are $\{G_1 = IIIXXX, G_2 = IXXIIX, G_3 = XIXIXIX, G_4 = IIIZZZZ, G_5 = IZZIZZZ, G_6 = ZIZIZIZ\}$ and the logical Pauli- X and Pauli- Z operations are $XXXXXXX$ and $ZZZZZZZ$ respectively. Thus the computational basis for the logical space would be $\{|0_L\rangle, |1_L\rangle\}$ where,

$$\begin{aligned} |0_L\rangle &= \frac{1}{2\sqrt{2}}(|0000000\rangle + |1010101\rangle + |0110011\rangle + |1100110\rangle + |0001111\rangle + |1011010\rangle + |0111100\rangle + |1101001\rangle) \\ |1_L\rangle &= \frac{1}{2\sqrt{2}}(|1111111\rangle + |0101010\rangle + |1001100\rangle + |0011001\rangle + |1110000\rangle + |0100101\rangle + |1000011\rangle + |0010110\rangle) \end{aligned} \quad (\text{D1})$$

Syndrome ($G_1G_2G_3G_4G_5G_6$)	Type of Error	Correction Operation
000000	No Error	$IIIIII$
000001	$B1$	$XIIIIII$
000010	$B2$	$IXIIII$
000011	$B3$	$IIXIIII$
000100	$B4$	$IIIIXII$
000101	$B5$	$IIIIIXII$
000110	$B6$	$IIIIIXI$
000111	$B7$	$IIIIIXX$
001000	$P1$	$ZIIIIII$
010000	$P2$	$IZIIII$
011000	$P3$	$IIZIIII$
100000	$P4$	$IIIIZII$
101000	$P5$	$IIIZIZI$
110000	$P6$	$IIIIIZI$
111000	$P7$	$IIIIIZZ$

Table I. Error correction using 7-qubit Steane code. A single qubit error can be detected and corrected from syndrome measurement. The measurement results and the corresponding correction operations are given here. BN and PN denotes bit-flip and phase-flip errors on N -th qubit.

A single-qubit error can be easily detected and corrected using the Steane code. Table I shows the syndrome measurement results and the corresponding error type along with the correction operations.

Appendix E: Encoding and decoding of Toric code

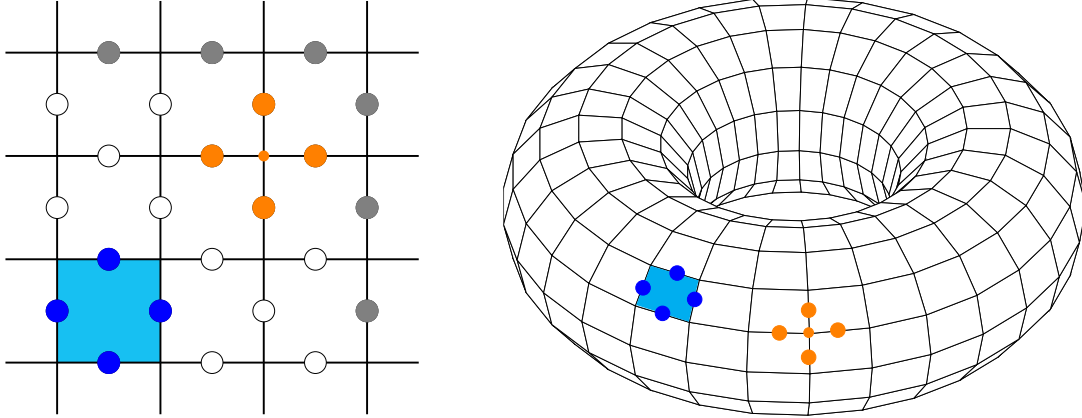


Figure 8. Lattice representation of Toric code ($L = 3$) and its embedding into a three-dimensional torus. Circles denote qubits, with gray circles as repeated qubits on boundaries. Vertices and plaquettes are duals of each other, and they denote stabilizers of the code. Two of such stabilizers are shown here in cyan (plaquette) and orange (vertex). One stabilizer is given by applying Pauli- Z on the qubits (shown in blue) adjacent to the plaquette, and the other is given by applying Pauli- X on the qubits adjacent to the vertex.

The toric code [63] is a $[[2L^2, 2, L]]$ QEC code, corresponding to an $L \times L$ lattice. Here, 2 logical qubits are encoded using $2L^2$ physical qubits with code distance L . Therefore this code can detect any $L - 1$ -qubit error and correct up to $\lfloor \frac{L-1}{2} \rfloor$ -qubit error. A lattice and a three-dimensional torus representation are given in Fig. 8 for $L = 3$. This is a stabilizer code. The stabilizer generators are given by applying Pauli- Z on each qubit adjacent to the plaquettes and Pauli- X on each qubit adjacent to the duals of the plaquettes. As the vertices are the duals of the plaquettes, Pauli- X can be applied on the qubits adjacent to the vertices to get stabilizer generators. These are the plaquette and the vertex (star) operators, respectively. In Fig. 8, one plaquette operator and one vertex operator are shown in blue and red, respectively. There are $L^2 - 1$ generators of each type, totaling $2(L^2 - 1)$ generators. The logical Pauli operators are given by non-trivial loops. There are a total of 5 independent loops in a torus. Out of that one is trivial, which can be deformed into a point without breaking it, giving the identity operator. The other four independent loops shown in Fig. 9 give four independent logical Pauli operators.

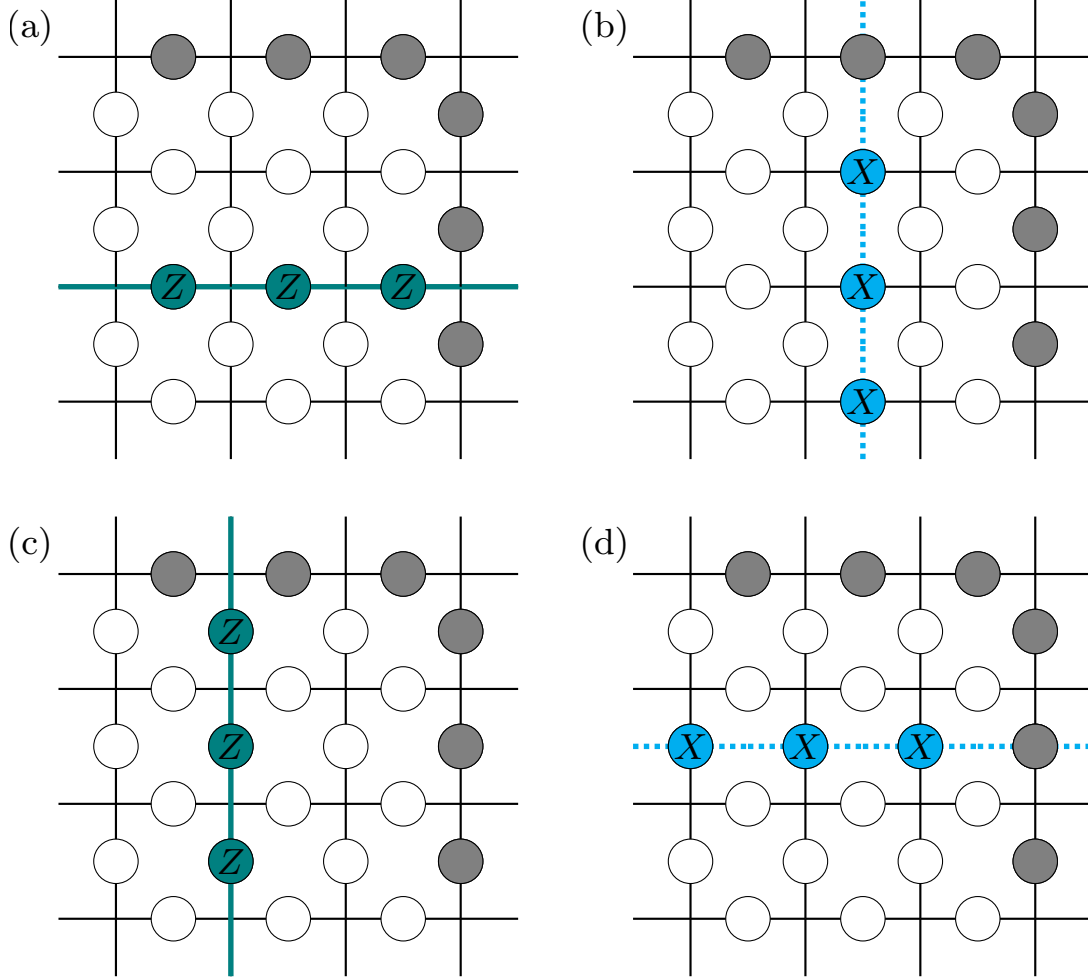


Figure 9. Four non-trivial independent loops in a 3×3 toric code representing four logical Pauli operators: (a) Z_1 , Logical Z operator for qubit 1; (b) X_1 , Logical X operator for qubit 2; (c) Z_2 , Logical Z operator for qubit 1; (d) X_2 , Logical X operator for qubit 2.

Syndrome ($G_1 G_2 G_3 G_4 G_5 G_6$)	Type of Error	Correction Operation
000000	No Error	IIIIII
000001	$B7, B8$	IIIIIXI, IIIIIIX
000010	$B2, B6$	IXIIIIII, IIIIIXII
000101	$B1, B5$	XIIIIII, IIIIXIII
000110	$B3, B4$	IIXIIII, IIIXIIII
001000	$P5, P6$	IIIZIIII, IIIIZII
010000	$P4, P8$	IIIZIIII, IIIIIIZ
101000	$P3, P7$	IIZIIII, IIIIIIZI
110000	$P1, P2$	ZIIIIII, IZIIIIII

Table II. Error correction using $[[8, 2, 2]]$ Toric code. The measurement results and the corresponding correction operations are given here. BN and PN denotes bit-flip and phase-flip errors on N -th qubit.

For $L = 2$, $2(2^2 - 1) = 6$ generators are $\{G_1 = XXXIIIXI, G_2 = XXIXIIIX, G_3 = IIXIXXXI, G_4 = ZIZZZIII, G_5 = IZZZIZII, G_6 = ZIIIIZZZ\}$. The logical Pauli operators are given by $\{Z_1 = ZZIIIIII, X_1 = XIIIXIII, Z_2 = IIZIIIZI, X_2 = IIXXIIII\}$. The computational basis for the code is given by

$\{|00\rangle_L, |01\rangle_L, |10\rangle_L, |11\rangle_L\}$ where,

$$\begin{aligned}
 |00\rangle_L &= \frac{1}{2\sqrt{2}} [|0\rangle + |29\rangle + |46\rangle + |51\rangle + |204\rangle + |209\rangle + |226\rangle + |255\rangle], \\
 |01\rangle_L &= \frac{1}{2\sqrt{2}} [|68\rangle + |89\rangle + |106\rangle + |119\rangle + |136\rangle + |149\rangle + |166\rangle + |187\rangle], \\
 |10\rangle_L &= \frac{1}{2\sqrt{2}} [|3\rangle + |30\rangle + |45\rangle + |48\rangle + |207\rangle + |210\rangle + |225\rangle + |252\rangle], \\
 |11\rangle_L &= \frac{1}{2\sqrt{2}} [|71\rangle + |90\rangle + |105\rangle + |116\rangle + |139\rangle + |150\rangle + |165\rangle + |184\rangle]
 \end{aligned} \tag{E1}$$

The syndrome measurement results and the corresponding correction operations are given in Table II. From this table, it can be seen that for each error syndrome, there are two possible errors and two possible correction operations. Therefore, it is not possible to correct the error completely. One possible way may be the random application of the correction operators with a probability of 0.5. However, it being a probabilistic approach, it cannot ensure error correction. By taking $L \geq 3$, $\lfloor \frac{L-1}{2} \rfloor \geq \lfloor \frac{3-1}{2} \rfloor = 1$ -qubit error correction can be ensured.

Appendix F: Comparative analysis of the different QEC codes

Here, we provide a detailed analysis of how various QEC codes can be used to reconstruct the original system state when it interacts with a bosonic bath (Fig. 10–13). We examine this recovery process for different choices of initial states and systematically compare the performance of the codes in both weak- and larger-coupling regimes, considering in each case the limiting behaviors at low and high temperatures.

In Fig. 14 we provide an analysis of how the five-qubit code with multiple cycles performs for the Werner state $p|\psi^-\rangle\langle\psi^-| + (1-p)\frac{I}{4}$ for $p = 0.7$. We consider coupling strengths $\kappa/\omega = 0.01$ for the weak coupling limit and $\kappa/\omega = 0.1$ for the larger system-bath coupling, each with temperature $T = 0.2$ and 10.

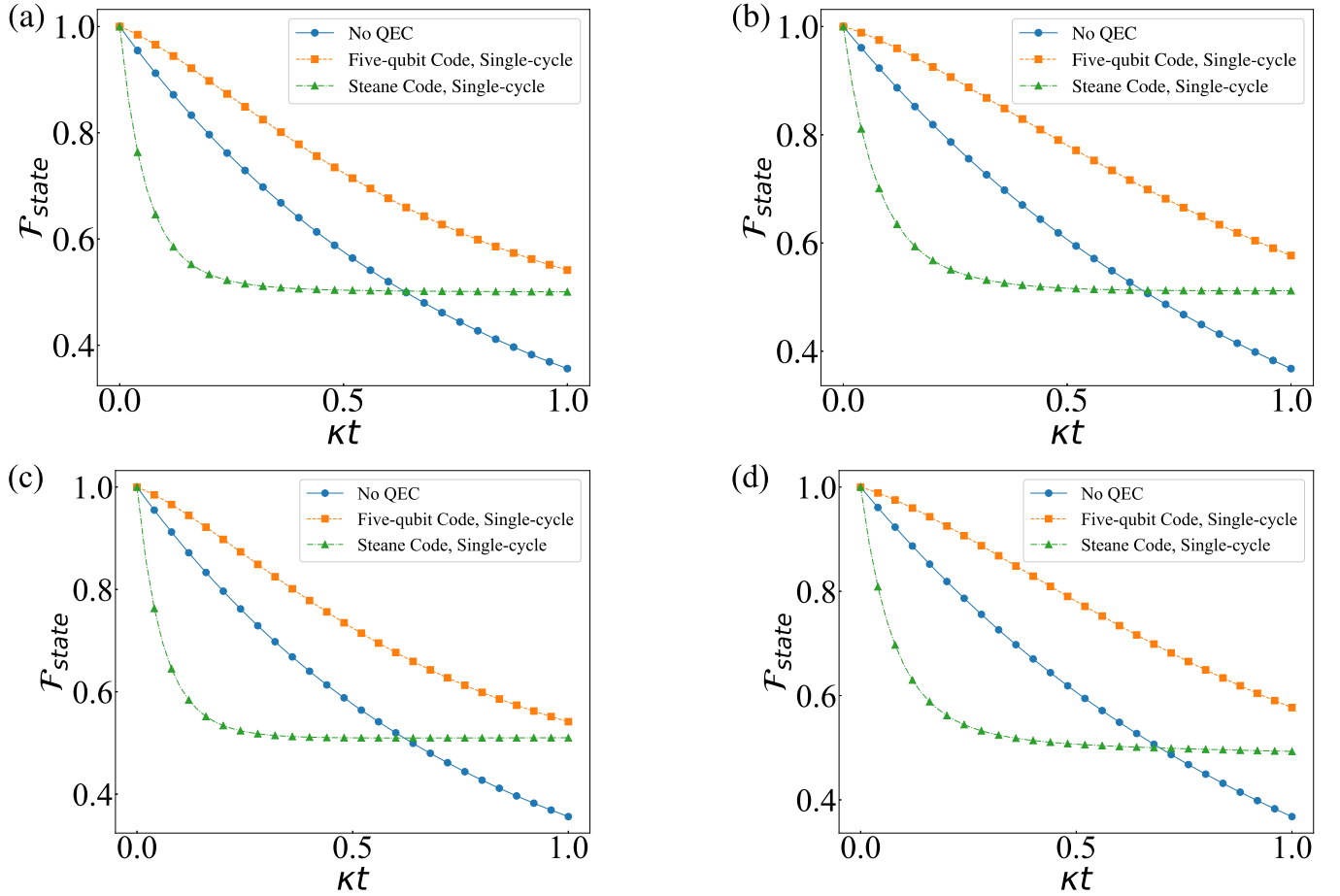


Figure 10. State fidelity \mathcal{F}_{state} of the initial state $|0\rangle$ with five-qubit QEC and Steane code. All qubits are coupled to baths with coupling strength $\kappa/\omega = 0.01$ with the bath temperature (a) $T = 10$, and (b) $T = 0.2$. (c) All qubits are coupled to baths with coupling strength $\kappa/\omega = 0.1$ and the temperature $T = 10$. (d) All qubits are coupled to baths with coupling strength $\kappa/\omega = 0.1$ and the temperature $T = 0.2$. The plot shows that the five-qubit code performs better than the Steane code.

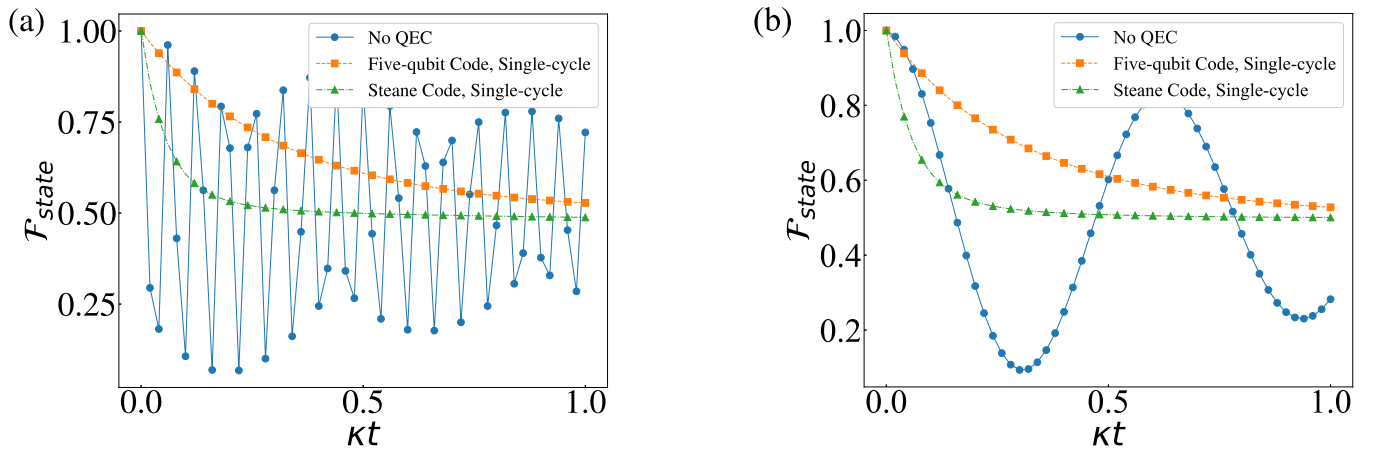


Figure 11. State fidelity \mathcal{F}_{state} of the initial state $|+\rangle$ with five-qubit QEC and Steane code. All qubits are coupled to baths with temperature $T = 10$ for coupling strengths (a) $\kappa/\omega = 0.01$, and (b) $\kappa/\omega = 0.1$. The plot shows that the five-qubit code performs better than the Steane code.

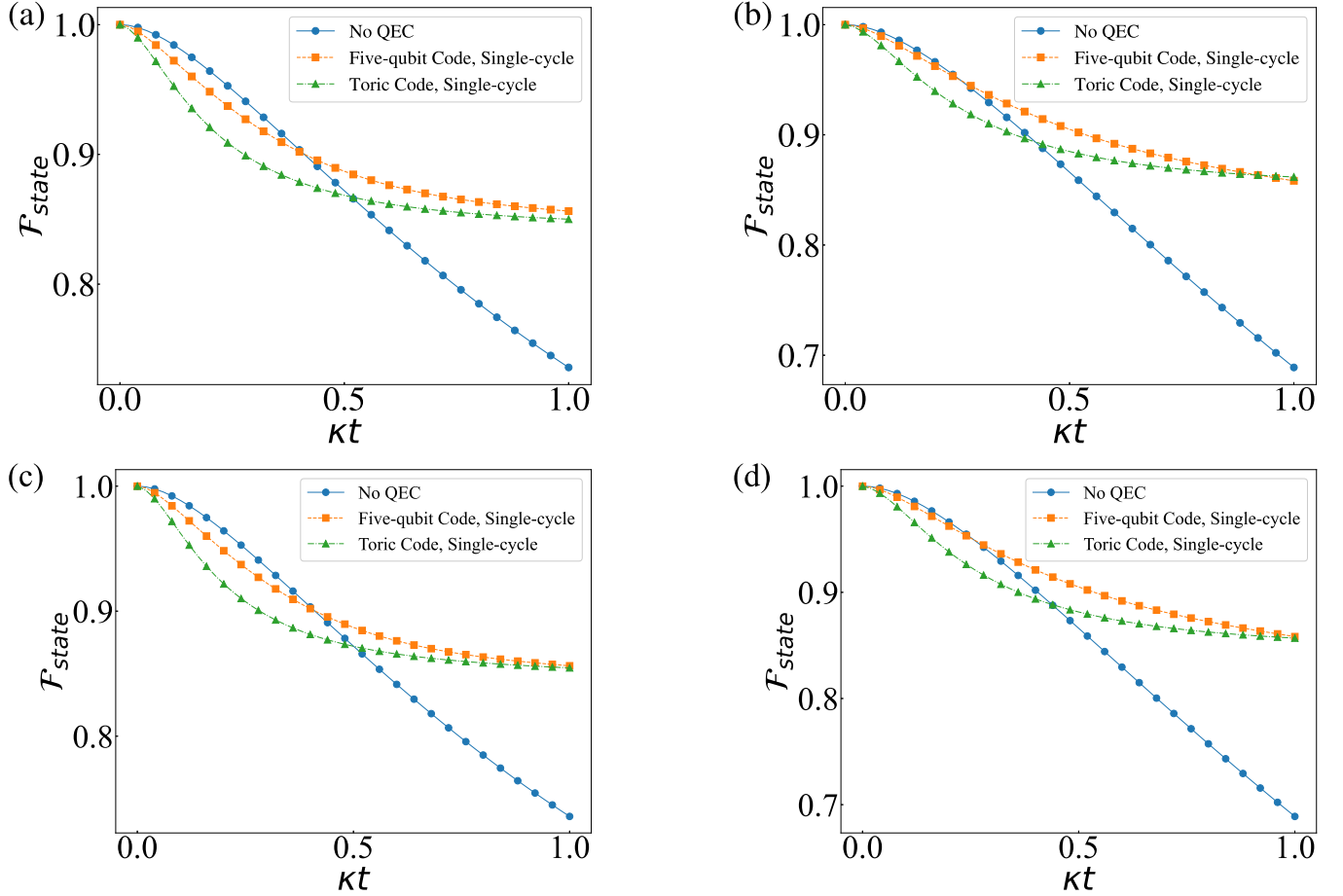


Figure 12. State fidelity \mathcal{F}_{state} of the initial state $p |\psi^-\rangle\langle\psi^-| + (1-p) \frac{I}{4}$ for $p = 0.5$ with five-qubit QEC and Toric code. (a) All qubits are coupled to baths with coupling strength $\kappa/\omega = 0.01$, with the bath temperature (a) $T = 10$ and (b) $T = 0.2$. For coupling strength $\kappa/\omega = 0.1$ with the bath temperature (c) $T = 10$ and (d) $T = 0.2$. The plot shows that the five-qubit code performs better than the Toric code.

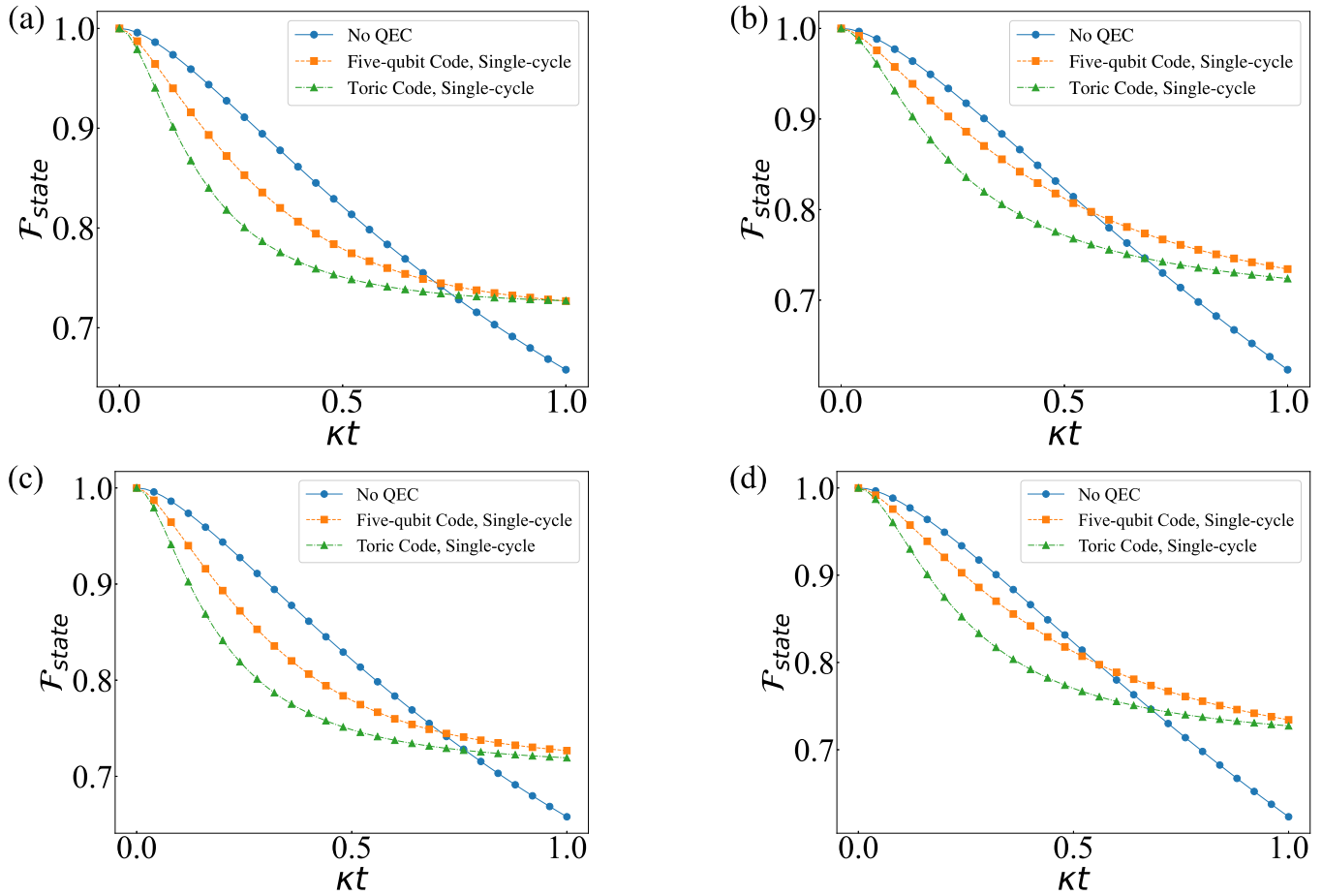


Figure 13. Same as Fig. 12 for $p = 0.7$.

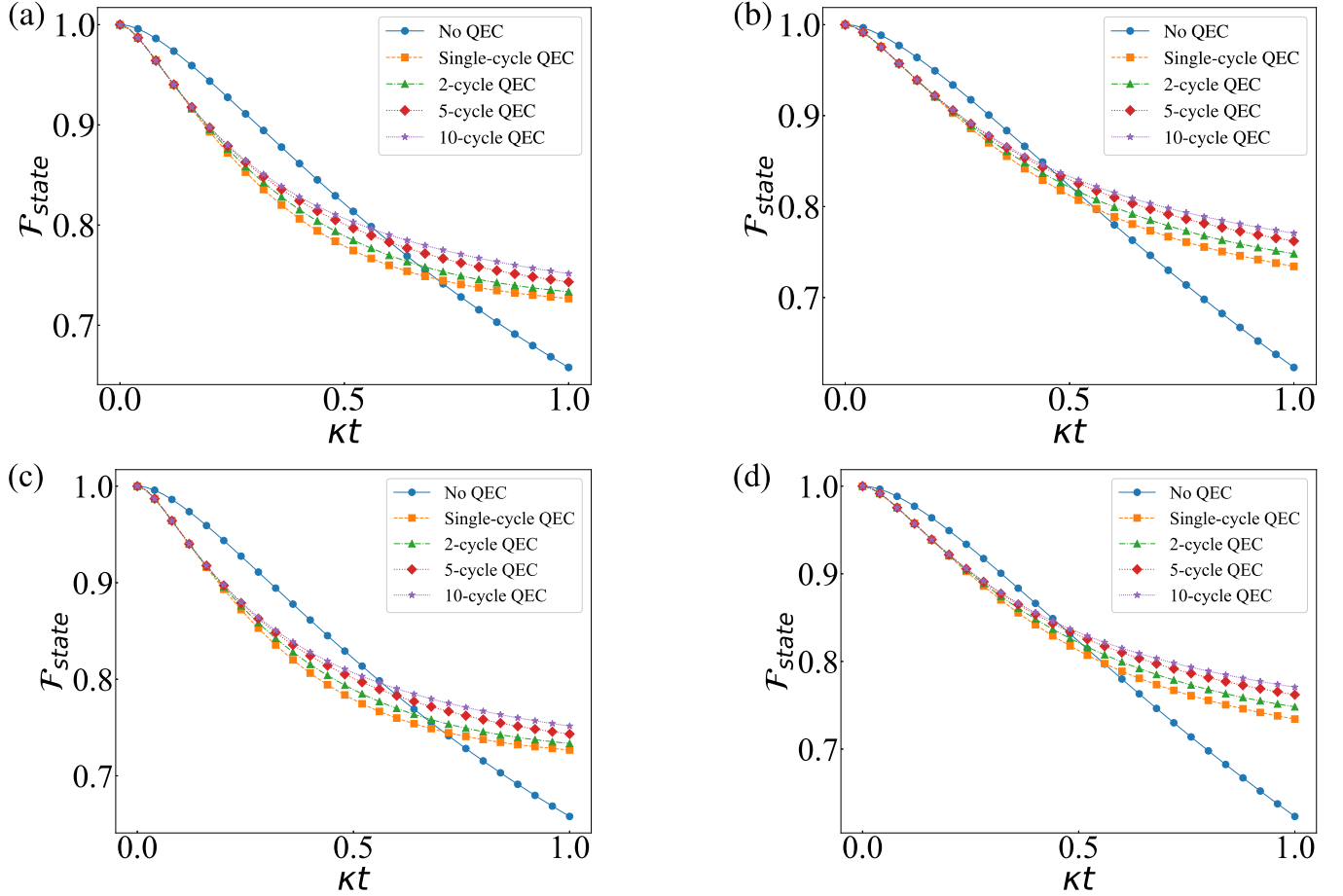


Figure 14. State fidelity $\mathcal{F}_{\text{state}}$ of the initial state $p |\psi^-\rangle\langle\psi^-| + (1-p) \frac{I}{4}$ for $p = 0.7$ with and without five-qubit QEC. We have considered QEC with single as well as multiple cycles for the number of cycles as 2, 5, and 10. All qubits are coupled to baths with coupling strength $\kappa/\omega = 0.01$, with the bath temperature (a) $T = 10$, and (b) $T = 0.2$. For coupling strength $\kappa/\omega = 0.1$ with the bath temperature (c) $T = 10$, and (d) $T = 0.2$. It is clear from the plot that as the number of QEC cycles increases, the fidelity also increases.